



AFRL-OSR-VA-TR-2014-0279

Carbohydrate Nanotech Hierarchical Assemblies UbX'bzCfa Uhcb'DfcWggib[of Oligosaccharide

**5XUm Braunschweig
UNIVERSITY OF MIAMI**

**09/17/2014
Final Report**

DISTRIBUTION A: Distribution approved for public release.

Air Force Research Laboratory
AF Office Of Scientific Research (AFOSR)/ RTD
Arlington, Virginia 22203
Air Force Materiel Command

REPORT DOCUMENTATION PAGE

Form Approved
OMB No. 0704-0188

Public reporting burden for this collection of information is estimated to average 1 hour per response, including the time for reviewing instructions, searching existing data sources, gathering and maintaining the data needed, and completing and reviewing this collection of information. Send comments regarding this burden estimate or any other aspect of this collection of information, including suggestions for reducing this burden to Department of Defense, Washington Headquarters Services, Directorate for Information Operations and Reports (0704-0188), 1215 Jefferson Davis Highway, Suite 1204, Arlington, VA 22202-4302. Respondents should be aware that notwithstanding any other provision of law, no person shall be subject to any penalty for failing to comply with a collection of information if it does not display a currently valid OMB control number. **PLEASE DO NOT RETURN YOUR FORM TO THE ABOVE ADDRESS.**

1. REPORT DATE (DD-MM-YYYY) 30/09/2014			2. REPORT TYPE FINAL REPORT		3. DATES COVERED (From - To) 07/01/2013-06/30/2014
4. TITLE AND SUBTITLE CARBOHYDRATE NANOTECH:HIERARCHICAL ASSEMBLIES AND INFORMATION PROCESSING FROM OLIGOSACCHARIDE-SYNTHETIC LECTIN HOST-GUEST			5a. CONTRACT NUMBER FA9550-13-1-0188		
			5b. GRANT NUMBER		
			5c. PROGRAM ELEMENT NUMBER		
6. AUTHOR(S) BRAUNSCHWEIG, ADAM B; BIAN, SHUDAN; XU, HAN			5d. PROJECT NUMBER		
			5e. TASK NUMBER		
			5f. WORK UNIT NUMBER		
7. PERFORMING ORGANIZATION NAME(S) AND ADDRESS(ES) UNIVERSITY OF MIAMI RESEARCH ADMINISTRATION - CORAL GABLES 1551 BRECIA AVE RM 100A CORAL GABLES FL 33146-2503			8. PERFORMING ORGANIZATION REPORT NUMBER		
9. SPONSORING / MONITORING AGENCY NAME(S) AND ADDRESS(ES) DR. HUGH DELONG AFOSR 875 N RANDOLPH ST, RM 3112 ARLINGTON, VA 22203			10. SPONSOR/MONITOR'S ACRONYM(S) AFOSR		
			11. SPONSOR/MONITOR'S REPORT NUMBER(S)		
12. DISTRIBUTION / AVAILABILITY STATEMENT A = Approved for public release; distribution is unlimited					
13. SUPPLEMENTARY NOTES					
14. ABSTRACT The information capacity of oligosaccharides greatly exceeds that of oligonucleotides or oligopeptides, but this property of carbohydrates is rarely accessed to create synthetic nanosystems. This project sought to use the information carrying capacity of oligosaccharides for creating hierarchical assemblies and for molecular information processing. Specifically, we have created new methods for printing multivalent carbohydrates with sub-micrometer feature diameters using a photochemically-controlled grafted-from brush polymerization strategy, and the resulting glycopolymers are orders-of-magnitude more sensitive towards lectins compared to their monomeric counterparts. In addition, we have expanded the surfaces that can be used to immobilize biological ligands to include graphene by developing a force-accelerated printing strategy, and in doing so, we have increased the understanding of force on surface reactions. Finally, we have developed a new, mannose-specific synthetic lectin that achieves selectivity using biomimetic cooperative and multivalent binding modes.					
15. SUBJECT TERMS					
16. SECURITY CLASSIFICATION OF: a. REPORT U			17. LIMITATION OF ABSTRACT UU	18. NUMBER OF PAGES	19a. NAME OF RESPONSIBLE PERSON ADAM B. BRAUNSCHWEIG
b. ABSTRACT U					19b. TELEPHONE NUMBER (include area code) (305) 284-2516
c. THIS PAGE U					

AFOSR Final Report

Carbohydrate Nanotechnology: Hierarchical Assemblies and Information Processing with Oligosaccharide-Synthetic Lectin Host-Guest Systems

Grant Number: FA9550-13-1-0188

Principal Investigator:
Adam B. Braunschweig
a.braunschweig@miami.edu
Phone: (305) 284-2516

Department of Chemistry
University of Miami
1301 Memorial Drive
Coral Gables, FL 33146

September 2014

Period covered by this report:

7/1/2013 to 6/30/2014

A. Introduction and Objectives

Self-assembly provides an attractive route from simple building blocks to hierarchical nanomaterials whose sophistication and function rival those found in living systems. Nature uses the cooperative and multivalent interactions between carbohydrates and the proteins that bind them, termed lectins, to direct the formation of larger aggregates, such as tissues, organs, and ultimately organisms. Despite their increased information density relative to other recognition elements (DNA base pairs, peptides, etc.) currently used to assemble hierarchical nanosystems (Table 1), carbohydrates

have not been adopted by researchers for organizing synthetic assemblies because natural lectins are too complex to use in the context of nanotechnology, and the intricacies of oligosaccharide structure makes designing specific hosts that can discriminate between different monosaccharides particularly difficult. While there is significant interest in developing synthetic lectins, this task remains challenging because monosaccharides contain several hydroxyl functions and multiple stereocenters per residue, and they typically occur as a constantly fluctuating mixture of 5- and 6-membered rings. However, the multivalency and cooperativity inherent to saccharide binding could add significant capabilities to synthetic nanotechnology. Both carbohydrates and lectins typically exist as multimeric assemblies, and the high affinity that arises from multivalent interactions leads to the error-correcting abilities that are characteristic of biological self-assembly. Moreover, binding in lectins can change as a function of the cooperativity that arises from the interplay of two or more interactions with the same receptor, so that the system as a whole behaves differently than the mere multiplication of individual interactions would predict. *The goal of the research program was to utilize oligosaccharide-synthetic lectin binding pairs to direct the assembly of self-organized, hierarchical materials and to employ the binding properties of these structures to create synthetic nanosystems for information storage and processing.* To that end, we pursued three synergistic objectives: (1) develop saccharide- synthetic lectin binding pairs that bind specifically and strongly through noncovalent interactions, (2) utilize the information encoded by the oligosaccharide structure to design advanced hierarchical materials for molecular logic operations, (3) employ cooperative and multivalent binding interactions between carbohydrates and synthetic lectins to drive mesoscopic assembly in solution, in polymers, and on surfaces. The major questions we asked were: How can we develop synthetic lectins that discriminate between monosaccharides that differ by only the orientation of a single hydroxyl? How can the conformational and binding dynamics inherent to saccharides be used in molecular logic? Can synthetic lectins employ multivalency and cooperativity to control the structure and dynamics of nanomaterials in three dimensions?

Table 1. Carbohydrate Information Density. The information density of biopolymers can be considered the number of different molecules (N) that can be made from an oligomer of a given size (S). For nucleotides, $N = 4^S$ and for peptides $N = 20^S$, but for carbohydrates the equation is far more complex.

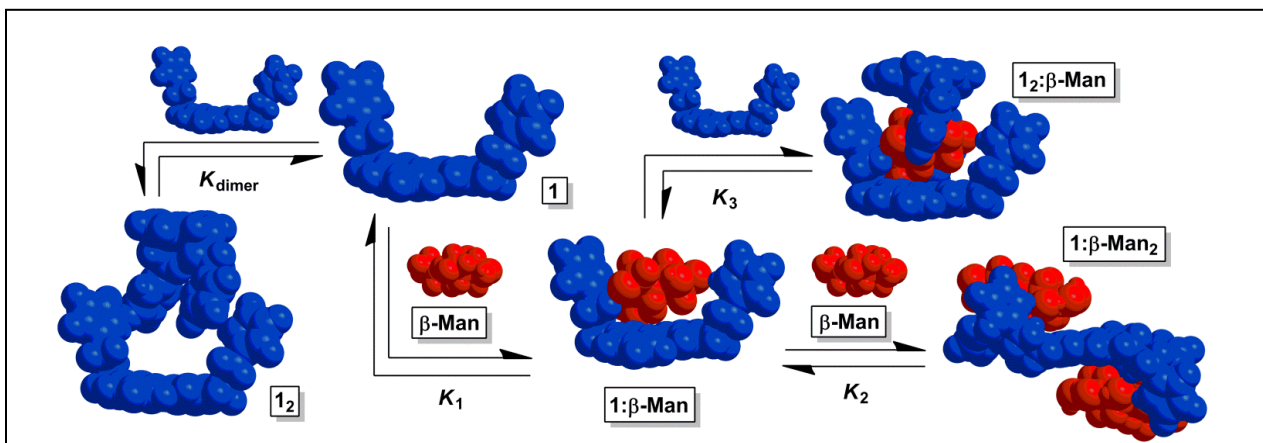
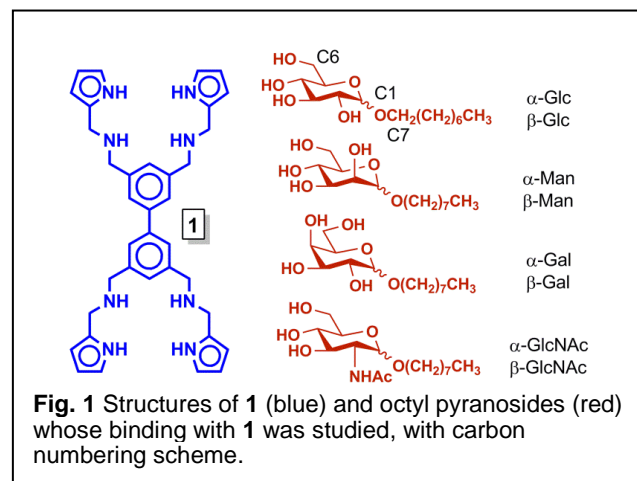
Number of Different Oligomers			
Oligomer Size	Nucleotides	Peptides	Carbohydrates
1	4	20	20
2	16	400	1,360
3	64	8,000	126,080
4	256	160,000	13,495,040
5	1,024	3,200,000	1,569,745,920
6	4,096	64,000,000	192,780,943,360

B. Progress Towards Major Research Goals

During the award period, the majority of the project goals were accomplished, and significant progress was made towards all research goals. We have developed a new, mannose-specific synthetic lectin scaffold that achieves specificity through cooperative and multivalent pathways (**Section C.1.**). The ability of this molecule to switch between targets and the complex molecular logic that drives this switching has been determined, and this is a successful demonstration of one of the major project goals: demonstration of a synthetic, carbohydrate based information processing system. Another major aim of the proposed work was to optimize new surface chemistries for immobilizing carbohydrates. To this end, we have developed the first chemistry to covalently pattern graphene using force-accelerated Diels-Alder reactions (**Section C.2.**), and this chemistry is compatible with carbohydrates. Subsequently, we used massively-parallel tip arrays to deliver light sight-specifically to a surface and thereby initiate photochemical brush polymerizations. This reaction methodology was used to create carbohydrate-containing brush polymers with binding affinity that is orders-of-magnitude greater than conventional glycan microarrays (**Section C.3.**). Because of the critical role that force plays in surface reactions, we have systematically and quantitatively investigated how force accelerates reactions on surfaces, and developed a new predictive model explaining previously contentious observations related to the force-accelerated Huisgen reaction (**Section C.4.**), which we have used previously to immobilize carbohydrates. Finally, we have continued to explore the dynamics of activated suspensions consisting of Au-Pt nanorods, and we have developed a model to describe their movement around microspheres (**Section C.5.**), and these studies will move us towards the goal of creating integrated carbohydrate-containing nanosystems with complexity of natural information carrying networks.

C. Results and Discussion

C.1. Synthetic Lectin Design. Natural saccharide-binding proteins, including lectins and periplasmic substrate-binding proteins, use water desolvation, hydrogen bonding (H-bonding), and C-H \cdots π interactions to selectively recognize glycans that may differ only by the orientation of a single hydroxyl group to achieve binding affinities, K_a s, as high at 10^6 M $^{-1}$. Selective carbohydrate recognition with artificial receptors remains a major area of investigation because of the challenge of differentiating between molecules with subtle structural differences, their ability to reveal fundamental aspects of saccharide binding, and their potential applications in disease detection, therapy, or catalysis. Mannose is a particularly interesting monosaccharide target because it is involved in signaling for several cancers, and as a consequence developing mannose specific synthetic receptors could reveal how carbohydrates are employed for communication purposes. The challenge with mannose as a target for any of these applications is that it is an epimer of glucose – the most prevalent monosaccharide in biology – and is thus very difficult to design receptors that can distinguish between molecules that differ only by the orientation around a single stereocenter. However, synthetic carbohydrate receptors with increased binding affinity, expanded substrate scope beyond all-equatorial glycosides, and increased selectivity continue to be a major research goal because of the new capabilities they could provide in terms of biological activity, sensing, and hierarchical assembly.



To address these challenges, we pursued an alternate design approach towards synthetic saccharide receptors that involves preparing a flexible host that does not possess rigid preorganization and as a result is capable of binding carbohydrates through pathways that arise from conformational rearrangements and positive homotropic cooperativity. Homotropic cooperativity – whereby an initial association of a target substrate induces conformational

restrictions that enhance further binding of the same substrate – has been employed previously in synthetic receptors to increase binding strength towards targets such as diacids and syndiols. However, synthetic receptors that utilize homotropic cooperativity remain rare, and few examples exist of hosts that rely upon cooperativity to enhance saccharide binding, despite the fact that cooperativity and multivalency are ubiquitous elements of carbohydrate recognition in biology. The advantages that could arise with carbohydrate receptors that employ positive allosteric cooperativity include (1) shorter synthetic sequences because specificity and affinity

are the direct result of allostery, (2) increased solubility associated with receptor flexibility, and (3) employing the same binding mechanisms as natural saccharide receptors could provide fundamental insights into the complex carbohydrate recognition motifs that are prevalent in nature. To this end, we have designed receptor **1** that contains aminopyrrolitic groups appended to a flexible scaffold with eight freely rotating methylene groups and a freely rotating biphenyl bond (Figure 1). Thus, **1** was designed to dynamically explore thermodynamic and conformational space and confirm that increased receptor flexibility can induce specificity for carbohydrate guests through allostery despite a higher entropic penalty experienced in an initial association step. Through the use of ^1H NMR titrations, we found that **1** achieves excellent selectivity for octyl mannosides through two allosteric cooperative pathways (Figure 2) with an overall selectivity as high as 16.8:1 α -Man: α -Gal in chloroform. Moreover, the selectivity is directly dependent on pyranoside concentration, where **1** binds preferentially to β -Glc at low concentration (<0.3 mM), then binds α - and β -Man at higher concentrations. To the best of our knowledge, **1** is the first synthetic carbohydrate receptor that (1) relies on cooperativity to increase selectivity and (2) whose selectivity switches with saccharide concentration.

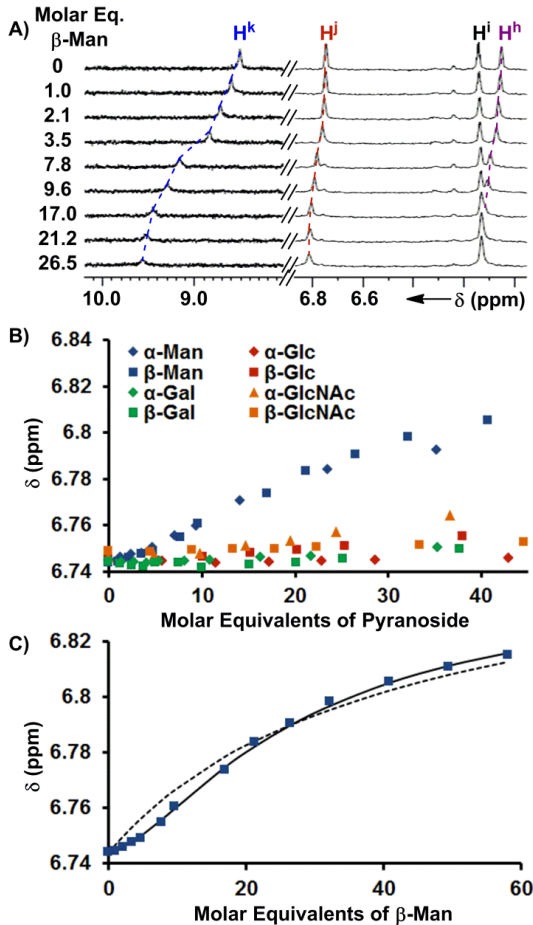


Fig. 3 a) ^1H NMR (600 MHz, CDCl_3 , 25°C) spectra obtained after the incremental addition of a 10.4 mM solution of β -Man to a 58.6 μM solution of **1**, with dashed lines illustrating the induced changes in chemical shifts. b) The chemical shift dependences of H^i of **1** (58.6 μM) is plotted as a function of molar equivalents of each of the eight added pyranosides from the ^1H NMR titrations. c) The fittings of the H^i chemical shift changes in response to the addition of β -Man to a model containing K_1 (dashed line) and $K_1 + K_2$ (solid line).

receptor selectivity were investigated by variable temperature ^1H NMR titrations in CDCl_3 . Chloroform facilitates the binding studies of new carbohydrate receptors because the solvent

does not compete for H-bonding between host and guest, thereby enhancing polar noncovalent bonds. These titrations revealed that the selectivity of **1** for octyl mannosides arises through a cooperative, multistep equilibrium (Figure 2). In solution, **1** exists as a dimer, **1**₂, that comes apart to form 1:1 complexes with the eight pyranosides with little selectivity. Upon altering the 1:pyranoside ratio from 1:1, two new mannoside-selective binding modes emerge that are both the result of positive cooperativity at 25°C. When the concentration of mannoside is increased, 1:2 receptor:pyranoside complexes form only with α -Man (**1**: α -Man₂) and β -Man (**1**: β -Man₂). If instead, the concentration of **1** increases with respect to pyranoside, a 2:1 receptor:monosaccharide complex forms only with β -Man (**1**₂: β -Man). To understand the origin of the preferential binding of mannosides by **1**, these binding stoichiometries and the structures of **1**₂: β -Man, **1**: α -Man₂, and **1**: β -Man₂ were established through a variety of 1D and 2D NMR methods, and all values of K_1 , K_2 , K_3 , ΔH° and ΔS° were determined for each of these equilibria.

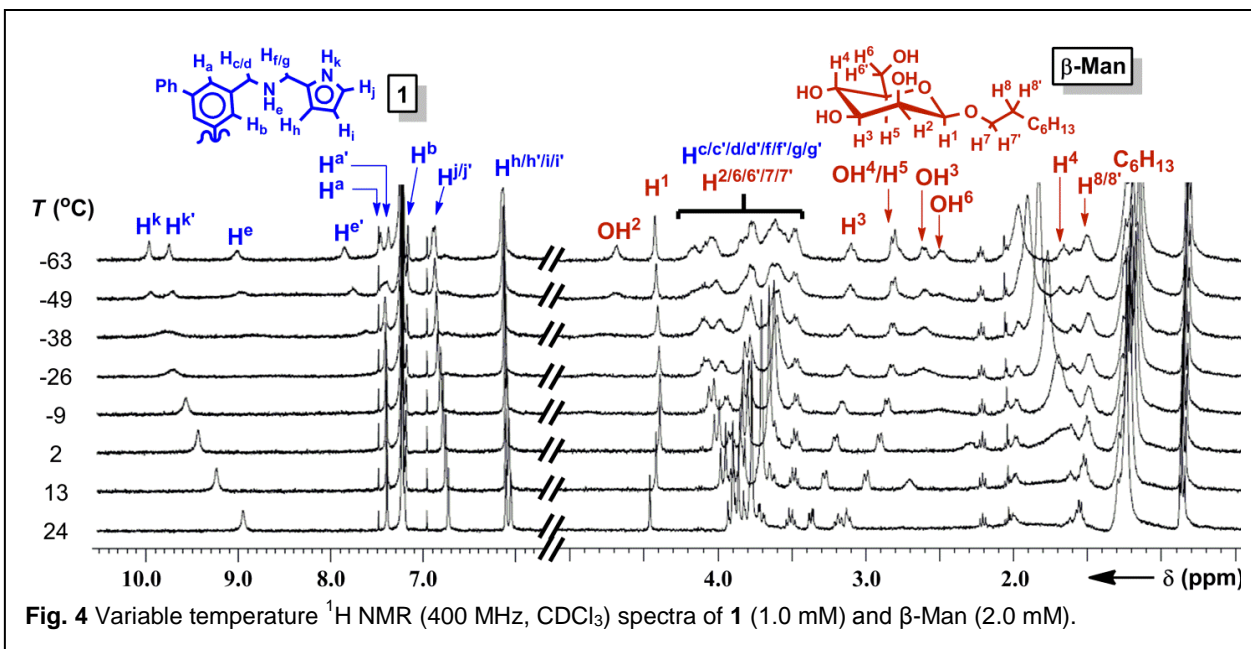


Fig. 4 Variable temperature ^1H NMR (400 MHz, CDCl_3) spectra of **1** (1.0 mM) and β -Man (2.0 mM).

1:2 Receptor:pyranoside binding

The binding of pyranosides was first studied under conditions where receptor **1** was maintained at a low concentration (<70 μM) to minimize the contribution of the K_{dimer} and K_3 equilibria (Figure 2). Once the values of K_1 and K_2 were determined, their values were held invariant in subsequent peak shift fittings, which facilitated the quantification of the other K_{a} s. The incremental addition of a 10-12 mM solution of each of the eight octyl pyranoside to a dilute solution of **1** (58.6 μM) induced changes in the ^1H NMR chemical shifts corresponding to the protons of **1**, owing to a fast exchange between bound and unbound substrates on the NMR timescale (Figure 3A). Notably, the change of mannoside proton chemical shifts, $\Delta\delta$, was significantly greater than the other pyranosides, suggesting that the overall binding free energy, ΔG° , was greater for mannosides than other pyranosides (Figure 3B). When the observed chemical shifts were plotted against the molar equivalents of pyranoside (Figure 3C), the observed perturbations for the mannoside protons follow a sigmoidal pattern, indicating that multiple equilibria in addition to 1:1 complexation are occurring in the titration. The titration induced peak shifts occurring upon addition of both anomers of glucose (α/β -Glc), galactose

(α / β -Gal), and N-acetylglucosamine (α / β -GlcNAc) produced no such sigmoidal curve and instead follow the hyperbolic shape of a 1:1 binding isotherm (Figure 3B). Since the concentration of pyranosides was intentionally kept low, the saturation region of the binding isotherm was only reached for the mannosides (Figure 3C), thus K_1 could not be determined for the other pyranosides from these experiments, although we were able to obtain these values by titrating **1** into solutions of pyranoside.

The chemical shift changes that occur because of the interaction of **1** with α - and β -Man were subjected to a global nonlinear fitting analysis with a model incorporating K_{dimer} , K_1 , and K_2 , and satisfactory fits to the $\Delta\delta$ s were obtained to provide macroscopic K_a s indicating the presence of 1:2 receptor:mannoside complexes **1**: α -Man₂ and **1**: β -Man₂. For an allosteric receptor possessing two equivalent binding sites, the experimentally measured K_a s must be corrected for the existence of two identical 1:1 intermediates to obtain microscopic association constants that accurately describe the association of each binding site. Since there are two identical pathways by which α / β -Man can associate with **1** to form a 1:1 complex, the macroscopic K_a for the first association process was divided by 2 to obtain microscopic association constant K_1 . Likewise, as there are two identical pathways for dissociation in **1**:Man₂, the macroscopic K_a for the second association process was multiplied by 2 to obtain microscopic association constant K_2 (Table 2). The interaction parameter, α , is the ratio of a microscopic K_a in the presence of cooperativity over its value in the absence of cooperativity, or reference K_a , and is a quantitative measure of cooperativity. Since both binding sites are identical, the reference K_a is equivalent to K_1 and thus $\alpha = K_2 / K_1$. An α value greater than 1 indicates that the first association event enhances the second, i.e. positive cooperativity. Likewise, the binding is negatively cooperative if α is less than 1, and the binding is non-cooperative if α is equal to 1. From an analysis of the microscopic K_a s, α -Man and β -Man were both found to possess α values of 13.7 and 7.6 respectively with receptor **1**, indicating a high degree of positive cooperativity occurs between **1** and both mannosides (Table 3).

The thermodynamic origin of this positive allosteric cooperativity in the formation of **1**: β -Man₂ was investigated by determining ΔH° and ΔS° associated with each binding step. The ¹H NMR titrations between **1** and β -Man were repeated at 20, 15, and 10°C, and K_1 and K_2 values for each temperature were obtained and subjected to Van't Hoff analyses to provide the thermodynamic parameters associated with each binding event. Notably, the ΔH° s of association

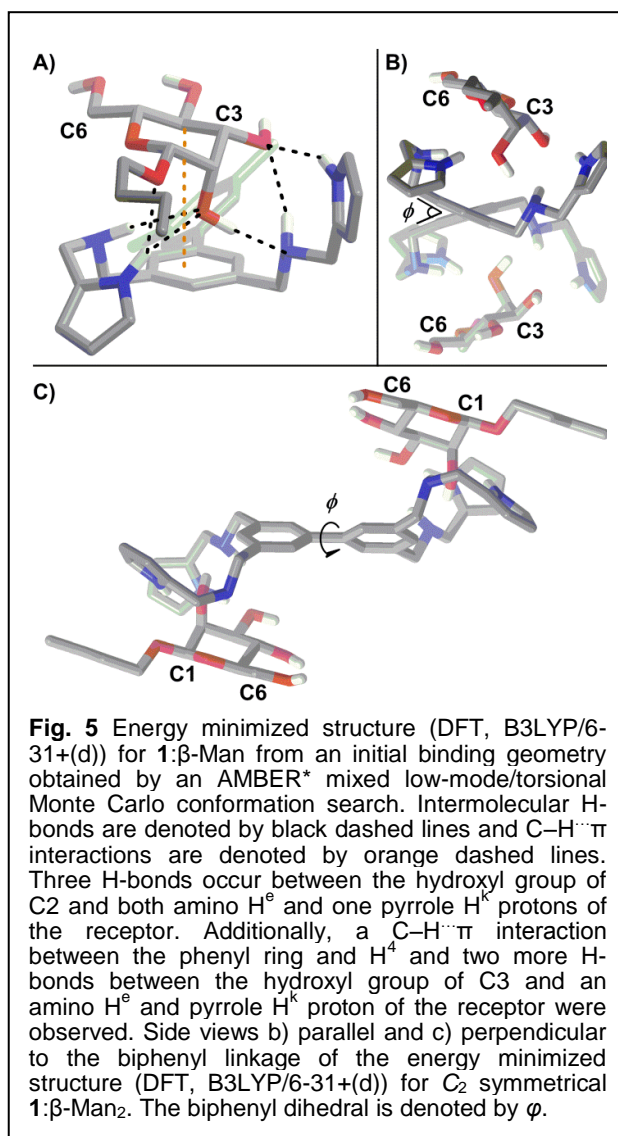
Table 2. Binding constants (K_a s, 25°C) and thermodynamic parameters (ΔH° , ΔS°) associated with the 1:1 (upper value), 1:2 (middle value), and 2:1 (lower value) **1**:pyranoside binding stoichiometries determined by NMR titrations and the intrinsic median binding concentration BC_{50}^0 calculated from K_{dimer} , K_1 , K_2 , and K_3 for each pyranoside interacting with **1** in CDCl₃ at 25°C.

Glycoside	Log K	ΔH° (kcal mol ⁻¹)	ΔS° (e.u.)	BC_{50}^0 (mM)
α -Glc	2.75 ± 0.04	-12.5 ± 0.3	-29 ± 1	
	a	—	—	1.86 ± 0.16
	a	—	—	
β -Glc	3.16 ± 0.01	-16.5 ± 0.1	-41 ± 1	
	a	—	—	0.70 ± 0.02
	0.39^b	-6.6 ± 0.4	-21 ± 1	
α -Man	2.57 ± 0.19	c	c	
	3.71 ± 0.10	c	c	0.46 ± 0.05
	a	—	—	
β -Man	2.46 ± 0.31	-20.5 ± 0.8	-57 ± 3	
	3.34 ± 0.11	-20.2 ± 1.2	-52 ± 4	0.73 ± 0.10
	2.45 ± 0.09	-11.0 ± 0.4	-26 ± 2	
α -Gal	2.18 ± 0.02	-13.1 ± 0.5	-34 ± 2	
	a	—	—	7.74 ± 0.31
	a	—	—	
β -Gal	2.59 ± 0.03	-15.4 ± 0.8	-40 ± 3	
	a	—	—	2.74 ± 0.18
	a	—	—	
α -GlcNAc	2.53 ± 0.02	-11.4 ± 0.2	-26 ± 1	
	a	—	—	3.18 ± 0.14
	a	—	—	
β -GlcNAc	2.65 ± 0.05	-11.8 ± 0.5	-27 ± 4	
	a	—	—	2.37 ± 0.26
	a	—	—	

^a No detectable binding. ^b Estimated by extrapolation of a van't Hoff plot with the assumption $\Delta C_p = 0$. ^c Not determined.

for the first and second binding step are identical, -20.5 ± 0.8 and -20.2 ± 1.2 kcal mol⁻¹ respectively, suggesting that both equivalents of β -Man bind **1** with an identical number of noncovalent interactions and that the mannosides do not interact with each other when bound to **1**. A comparison of the corresponding ΔS° values indicates a decrease in the unfavorable ΔS° occurs in the second binding step compared to the first, -52 ± 4 and -57 ± 3 e.u. respectively.

The geometries of **1**: β -Man and **1**: β -Man₂ were determined by 1D and 2D ¹H NMR and computational modeling to understand the structural origin of the cooperative binding.



symmetrically equivalent, resulting in a **1**: β -Man₂ complex that exhibits C₂ symmetry. A configuration where each mannose binds to two aminopyrrolitic arms on the same aromatic ring would render both H^b protons of receptor **1** symmetrically equivalent. With NMR providing a general understanding of how β -Man sits within **1**, a molecular mechanics (AMBER*) Monte Carlo conformational search was utilized to model the binding geometry of the **1**: β -Man complex. The conformational searches yielded only one minimum energy structure for **1**: β -Man, which was further optimized using density functional theory (B3LYP/6-31G+(d)). The resulting

geometries of **1**: β -Man and **1**: β -Man₂ were determined by 1D and 2D ¹H NMR and computational modeling to understand the structural origin of the cooperative binding. The ¹H NMR spectrum of a solution of **1** (1 mM) and β -Man (2 mM) in CDCl₃ exhibits averaged signals for all protons at 25°C because of a fast exchange of the signals corresponding to **1**, β -Man, **1**: β -Man₂, and **1**: β -Man. Upon cooling, the ¹H NMR resonances corresponding to **1**, except H^b, decoalesce into two sets of peaks at -40°C (Figure 4), indicating a partial desymmetrization occurring with receptor **1**. No decoalescence was observed for the resonances corresponding to β -Man signals upon cooling the solution (Figure 4), suggesting that both equivalents of β -Man occupy identical chemical environments in the **1**: β -Man₂ complex. In the absence of β -Man, the signals corresponding to **1** in the ¹H NMR spectrum do not decoalesce at low temperature, but rather are broadened. Thus, the new signals that arise upon cooling of the mixed sample can be attributed to a complex consisting of **1** and β -Man. A comparison of the ¹H NMR spectra at -63°C with varying ratios of **1**: β -Man revealed that the broad signals corresponding to free **1** disappear when more than two molar equivalents of β -Man are present in solution, further confirming the 1:2 stoichiometry of the complex. The two sets of signals observed in the ¹H NMR spectrum at -63°C (Figure 4) for the receptor and only one for the mannose, indicate that both pyranosides are bound to two aminopyrrolitic arms of **1** and are

calculated structure (Figure 5A) is in excellent agreement with the experimental 1D ^1H NMR data.

The origin of the cooperativity in receptor **1** was examined computationally by varying the dihedral about the biphenyl bond (φ , Figure 5B/C) as this is the only dynamic element of the receptor that is shared by both binding sites. While desolvation contributes significantly to ΔS° , it is not the source of cooperativity as both binding sites and mannosides are solvated identically. A comparison of the DFT (B3LYP/6-31G+(d)) minimized structures corresponding to **1**, **1**: β -Man, and **1**: β -Man₂ revealed φ values of 40.2°, 38.5°, and 39.1° respectively, indicating that the contribution of torsional strain towards the observed cooperativity is negligible because φ in the bound state is close to the preferred φ of unbound **1**. More likely, the presence of a bound β -Man restricts the rotation about φ and incurs an entropic penalty that is only paid in the first association.

1:1 and 2:1 Receptor:pyranoside binding

The K_1 and K_3 of the binding of **1** to pyranosides were determined by titrating a solution of **1** (53.0 – 62.5 mM) into a 1.0 mM CDCl_3 solution of each octyl glycoside until a large excess of **1** was reached. Addition of **1** produced considerable changes in the ^1H NMR resonances of the receptor and all eight pyranosides (Figure 6A). For each non-mannoside, K_1 was determined by subjecting all resolvable resonances from each titration at 25°C to a global nonlinear fitting analysis with a model combining K_1 and K_{dimer} ($13.0 \pm 0.5 \text{ M}^{-1}$) (Table 3). Likewise, when the observed upfield chemical shift changes associated with α -Man were fit to a model incorporating K_{dimer} and the previously determined values of K_1 and K_2 , excellent fits for the peak shifts were obtained (Table 3). However, the peak shifts for the β -Man titration could only be fit accurately when the formation of a complex consisting of two molecules of **1** and one molecule of β -Man (**1**₂: β -Man, Figure 2) was considered (Figure 6B). The observed $\Delta\delta$ s were fit to a model consisting of K_{dimer} , K_1 , K_2 , and K_3 , with every binding constant except K_3 held invariant, to determine K_3 for β -Man. The values of $\log K_1$ for binding between **1** and all pyranosides range from 2.5 to 3.3 with the highest values associated with α - and β -Man and β -Glc. Importantly, little difference exists between the K_1 s for the eight pyranosides, indicating that little selectivity occurs in the first binding event. In contrast to the modest selectivity found in K_1 , 2:1 binding is only observed for β -Man at 25°C ($K_3 = 282 \text{ M}^{-1}$), although a value of $K_3 = 3 \text{ M}^{-1}$ for β -Glc can be extrapolated from a van't Hoff plot. Interestingly, a second receptor association does not occur with α -Man suggesting that the octyl

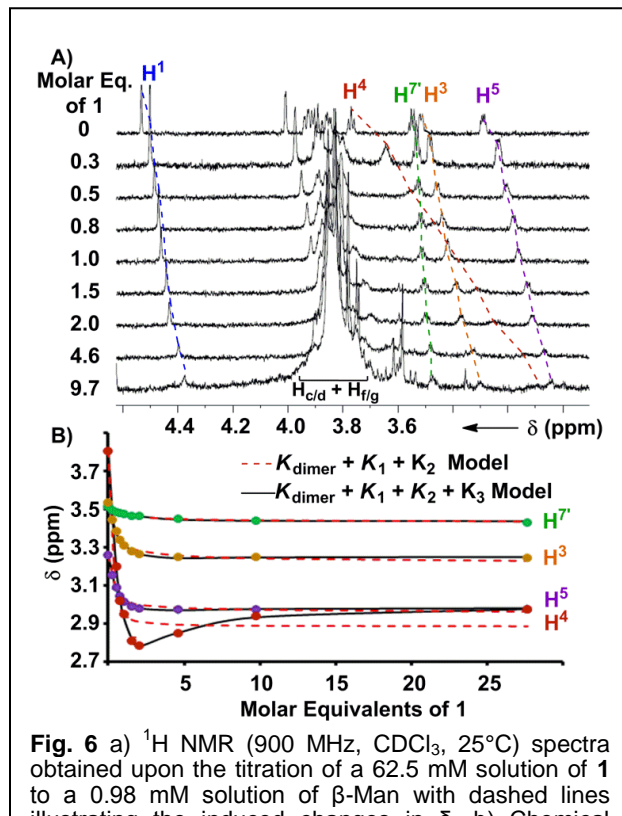
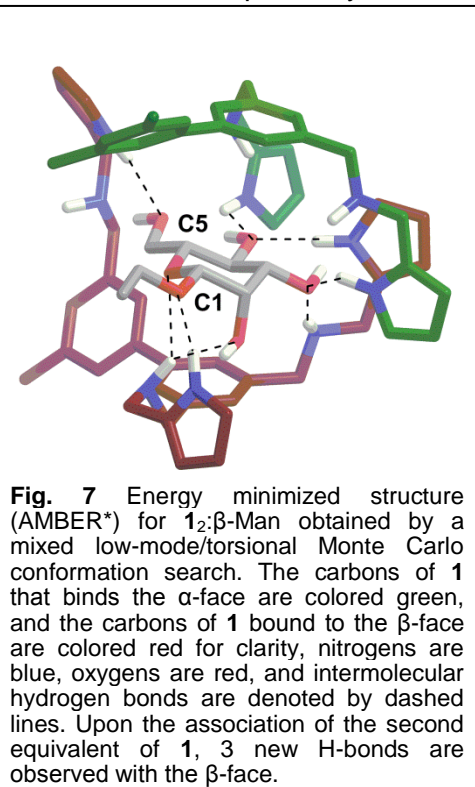


Fig. 6 a) ^1H NMR (900 MHz, CDCl_3 , 25°C) spectra obtained upon the titration of a 62.5 mM solution of **1** to a 0.98 mM solution of β -Man with dashed lines illustrating the induced changes in δ . b) Chemical shifts, δ , of β -Man as a function of molar equivalents of **1** at 5°C. The theoretical global fits with a model incorporating K_{dimer} , K_1 , and K_2 (dashed line) and with K_{dimer} , K_1 , K_2 , and K_3 (solid line) are shown.

chain at the anomeric position, which would be orientated away from the biphenyl base of **1** in **1**: α -Man (Figure 5A), interferes with the association of a second receptor.

The cooperativity that facilitates the formation of **1**₂: β -Man can be understood through the interaction parameter, α , which is the ratio between the values of K_3 in the presence and in the absence of cooperativity, the latter being the reference K_a . Since the two faces of β -Man are inequivalent, the two receptors do not bind to identical sites, thus K_1 is not an appropriate reference K_a . Rather, since K_3 describes the binding of the β -face of β -Man, which contains H¹, H³, and H⁵, in the presence of a receptor bound to the α -face, which contains H⁴, the reference K_a would describe the receptor binding to the β -face in the absence of a receptor bound to the α -face. From the -63°C ^1H - ^1H ROESY spectrum of **1**: β -Man₂, there are no observable NOEs between the pyranoside protons on the β -face and the biphenyl base of receptor **1**. Likewise, a ROESY spectrum performed at conditions that would produce significant quantities of the 1:1 **1**: β -Man complex revealed only a NOE between H⁴ of the α -face and H^a. Under these experimental conditions, a 1:1 binding event between **1** and the β -face does not occur to any appreciable extent, so an approximate baseline value of $K_a \leq 104 \text{ M}^{-1}$ was obtained. Thus, an estimated $K_3 \geq 282 \text{ M}^{-1}$ is evidence for positive cooperativity in K_3 with β -Man, with a corresponding α of at least 2.7.



To determine why K_3 occurs exclusively with β -Man at room temperature, ΔH° and ΔS° of association for each binding event between **1** and all pyranosides were obtained by repeating the ^1H NMR titrations at 20, 15, 10, and 5°C and subjecting the resulting K_a s to van't Hoff analyses (Table 3). All monosaccharides fit satisfactorily to a $K_{\text{dimer}} + K_1$ model at all temperatures, except for β -Man at all temperatures and β -Glc, at 15, 10, and 5°C , which required inclusion of the 2:1 receptor:pyranoside equilibrium (K_3) to achieve satisfactory fits to the titration data. When comparing the thermodynamic parameters for the formation of each 1:1 complex, a decrease in ΔH° occurs with a decrease in magnitude of ΔS° , which can be rationalized within the context of enthalpy-entropy compensation. Notably, the two β -monosaccharides with the highest 1:1 binding enthalpies, β -Man and β -Glc, are the only pyranosides that participate in K_3 . The large difference in ΔH° between **1**: β -Man and **1**: β -Glc, -20.5 and $-16.5 \text{ kcal mol}^{-1}$ respectively, suggests that the high selectivity in K_3 for β -Man is the result of **1** forming more noncovalent contacts with β -Man than with β -Glc, resulting in a more preorganized 1:1 complex. The ΔH° s for the formation of **1**₂: β -Glc and **1**₂: β -Man, -6.6 and $-11.0 \text{ kcal mol}^{-1}$ respectively, suggest that significantly more noncovalent contacts are formed in the latter, indicating that the selectivity for β -Man in the second binding event is enthalpically driven.

The binding geometries of **1**: β -Man and **1**₂: β -Man were determined and compared to understand how the preorganization of **1**: β -Man facilitates the formation of **1**₂: β -Man. A ^1H - ^1H ROESY experiment that was performed under conditions that favor the 1:1 complex (**1**: β -Man : **1**: β -Man₂ = 2 : 1.5) was consistent with the previously determined binding geometry for **1**: β -Man. Notably, in the **1**: β -Man geometry, a significant portion of β -Man is exposed to solvent

because one of the arms of **1** is orientated downwards underneath the n-octyl chain of β -Man, which provides a window for a second equivalent of **1** to bind onto the exposed β -face of β -Man. The structure of $1_2\beta$ -Man was determined by performing a ^1H - ^1H ROESY experiment with a concentrated 2:1 receptor:pyranoside CDCl_3 mixture at -10°C where $1_2\beta$ -Man would be the major species in solution. NOEs were observed between protons located on the biphenyl base and pyrroles, suggesting a geometry where one molecule of β -Man is engaged by two molecules of **1**, and the two molecules of **1** are in close contact. By using a similar AMBER* conformational search that was used to obtain the 1: β -Man structure, a $1_2\beta$ -Man structure was obtained (Figure 7) that is consistent with the thermodynamic data and the 1D and 2D ^1H NMR spectra. In contrast, the ^1H - ^1H ROESY of β -Glc and **1** under conditions that favor the 1:1 complex revealed that the axial protons on both faces of β -Glc have observable NOEs with the biphenyl base of **1**, indicating that more than one binding geometry exists at equilibrium since **1** cannot interact with both faces of β -Glc simultaneously. Because the entropic penalty for the preorganization of 1: β -Glc has not been paid, we speculate that the ΔS° associated with a second molecule of **1** binding to the 1:1 complex becomes prohibitively high, preventing the formation of a 2:1 complex. It should be noted that in the calculated structure of $1_2\beta$ -Man only three arms of each equivalent of **1** participate in binding to β -Man, so the fourth arms can be replaced in future receptors to increase function.

*Implications of competing equilibria on the selectivity of **1***

In the presence of β -Man, the 1:1 complex, **1**: β -Man, can either bind a second molecule of pyranoside, to form $1:\beta\text{-Man}_2$ (K_2), or **1**, to form $1_2\beta\text{-Man}$ (K_3). The outcome of these two competing processes is dependent on the concentrations of each substrate, with K_2 dominating at high concentrations of β -Man relative to **1**, whereas K_3 is preferred the presence of excess **1**. Thus, the numerous equilibria operating simultaneously in a solution of **1** and pyranoside (K_{dimer} , K_1 , K_2 and K_3) and the concentration dependence of cooperative binding complicate the analysis of the overall selectivity of **1** for the eight pyranosides. The BC_{50} values of each of the pyranosides – defined as the total concentration of receptor **1** needed to bind 50% of the available pyranosides in solution – were computed over a pyranoside concentration range of 0 to 10.0 mM to probe both the magnitude and concentration dependence of the selectivity of **1** for the eight pyranosides (Figure 8A). Note that all equilibria present in a receptor/pyranoside mixture contribute toward the calculated BC_{50} value, and a higher $1/\text{BC}_{50}$ value is indicative of a higher overall binding strength.

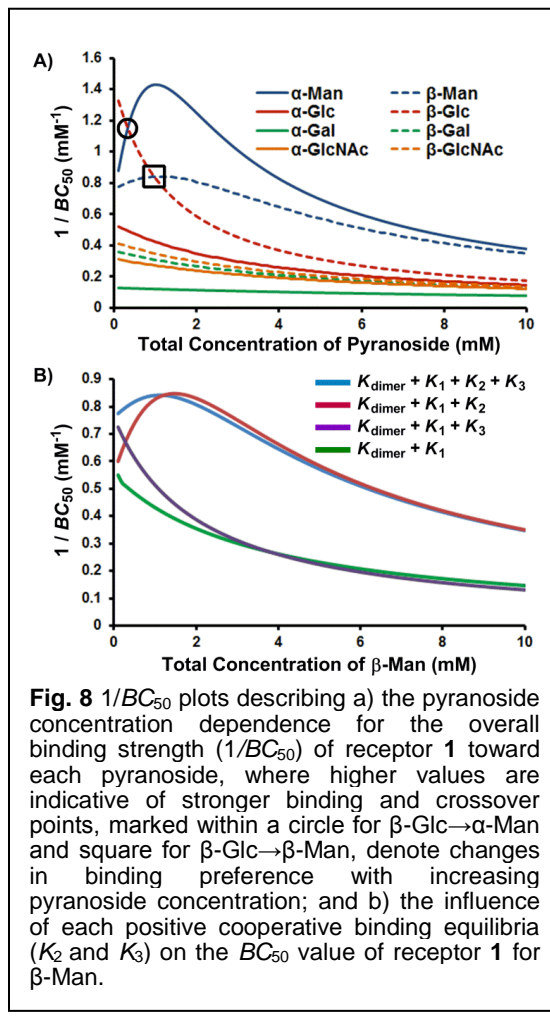


Fig. 8 $1/\text{BC}_{50}$ plots describing a) the pyranoside concentration dependence for the overall binding strength ($1/\text{BC}_{50}$) of receptor **1** toward each pyranoside, where higher values are indicative of stronger binding and crossover points, marked within a circle for $\beta\text{-Glc}\rightarrow\alpha\text{-Man}$ and square for $\beta\text{-Glc}\rightarrow\beta\text{-Man}$, denote changes in binding preference with increasing pyranoside concentration; and b) the influence of each positive cooperative binding equilibria (K_2 and K_3) on the BC_{50} value of receptor **1** for $\beta\text{-Man}$.

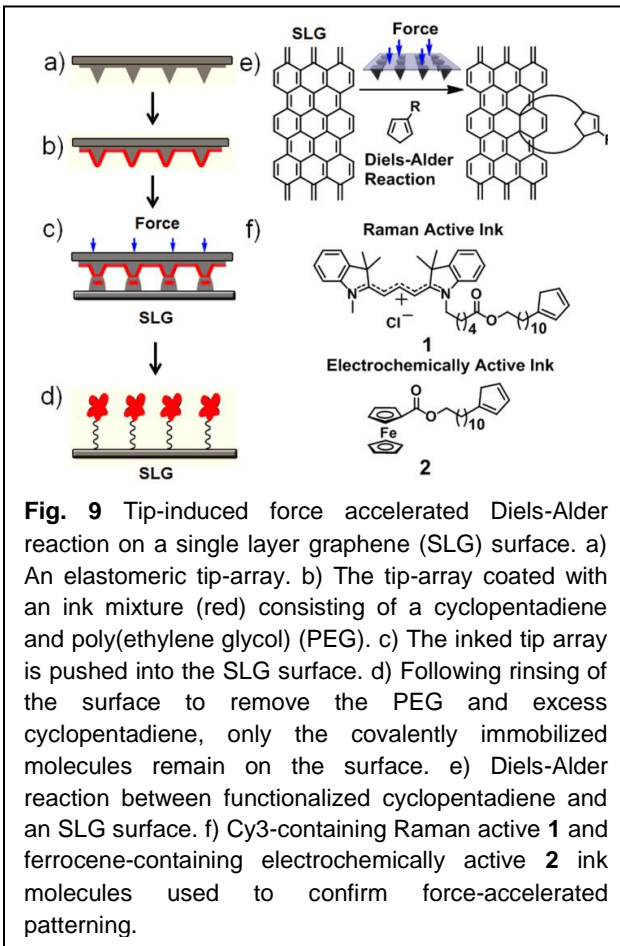
The $1/BC_{50}$ plots reveal the effects of positive cooperativity on the binding affinity of **1** toward mannosides. Molecules with K_2 possess parabolic curves in the $1/BC_{50}$ plot. This is particularly evident for α -Man which possesses the highest affinity for **1** compared to all other pyranosides at a 0.8 mM pyranoside concentration. Interestingly, for β -Man, which exhibits cooperativity in both K_2 and K_3 , a broader parabolic shape is observed, and little concentration dependence on the overall binding strength occurs between 0 and 4.0 mM of β -Man. When the calculated $1/BC_{50}$ plot is compared to a hypothetical plot in which only K_1 and K_3 are present, it was found that the presence of K_3 induces a substantial increase in selectivity at low concentrations (< 1.5 mM) of β -Man (Figure 8B). Alternatively, when a hypothetical plot is generated with only K_1 and K_2 , K_2 enhanced selectivity when $[\beta\text{-Man}]$ is greater than 1.0 mM, *thus demonstrating the direct contribution of cooperative, complex equilibria on selectivity in saccharide receptors* (Figure 8B). Moreover, these plots confirm that pyranoside concentration controls which equilibrium, i.e. K_2 or K_3 , prevails. At concentrations below 1.0 mM of β -Man, higher stoichiometry binding is achieved through K_3 , while at greater β -Man concentrations, K_2 dominates.

As each $1/BC_{50}$ plot is a measure of affinity between **1** and pyranosides, comparing the plots of two or more pyranosides provides a means of assessing selectivity. Thus, the concentration of α -Man where the maximum $1/BC_{50}$ value is obtained (0.8 mM) is also where the maximum selectivity occurs for α -Man relative to the other pyranosides. Beyond this value, the selectivities gradually approach 2:1 mannose:pyranoside, which is a consequence of the differences in binding stoichiometry – receptor **1** can accommodate two molecules of mannosides and only binds 1:1 for the other pyranosides. Importantly, crossover points in the BC_{50} plots are observed between β -Glc and the mannosides (Figure 8A), *meaning that the selectivity of **1** changes as a function of pyranoside concentration, which is a form of molecular logic, and a major goal of Y3*. At low pyranoside concentrations (< 0.3 mM), receptor **1** binds β -Glc with the highest affinity owing to its high value of K_1 , which effectively competes with the cooperative binding of **1** toward mannosides. From 0.3 mM to 1.0 mM, the binding order for **1** is α -Man > β -Glc > β -Man. At higher pyranoside concentrations (> 1.0 mM), the binding order for **1** changes to α -Man > β -Man > β -Glc as a result of the 2:1 binding stoichiometry that occurs only with mannosides. Consequently, a new concentration dependence has been discovered that governs the stoichiometry of the resulting complex and the pyranoside preference of the receptor.

Significance and outlook

The flexible receptor **1** achieves selectivity between pyranosides that may differ only by the orientation of a single hydroxyl group, despite the entropic penalty that must be paid to organize the complexes. In fact, the lack of preorganization in the strong **1**: β -Glc complex precludes the formation of a stable **1**₂: β -Glc structure, so entropy contributes significantly towards selectivity. Although receptor **1** does not achieve the same overall affinity as the best rigidly preorganized mannose-specific receptors, the selectivity is comparable despite the differences in binding mechanisms, thus confirming the hypothesis that increasing the receptor dynamics reveals new binding geometries because of the ability of flexible hosts to dynamically explore conformational space. Synthetic carbohydrate receptors can provide insight into the subtleties of natural lectin-carbohydrate interactions and reveal how carbohydrate recognition conveys complex information in biological networks. Eukaryotic cell surfaces are coated with a carbohydrate layer, the glycocalyx, where the multivalent presentation of carbohydrates on a cell surface enhances binding affinity, a phenomenon termed the cluster glycoside effect. Interestingly, the selectivity of **1** changes with pyranoside concentration, where **1** preferentially binds glucosides

at low concentration (<0.3 mM) and mannosides at higher concentrations that are similar to the increased localized concentrations present in mannoside clusters on cell surfaces. While concentration dependent selectivity may be unprecedented with synthetic carbohydrate receptors, multivalency and cooperativity are ubiquitous in biology, so concentration dependent switching may commonly occur with natural lectins and could have implications for hierarchical organization and information transfer in biological networks. This work (*Chemical Science*, **2013**, *4*, 357–367) represents the accomplishment of the major Y1 and Y2 goals with respect to synthetic lectins by creating a new receptor that engages cooperativity, a binding mode ubiquitous to natural lectins, to perform molecular logic operations.



suggested to us conditions that could be used to scalably pattern graphene at ambient temperatures and atmosphere. Because of their negative activation volumes, cycloaddition reactions are significantly accelerated in pressurized reaction vessels, thus, we reasoned that a localized force between SLG and a diene (Figure 9a) would accelerate the Diels-Alder reactions and thereby immobilize molecules site-specifically onto the basal plane of graphene through the formation of two new C–C bonds (Figure 9b).

To demonstrate that force accelerated cycloadditions could covalently pattern large areas ($\sim 1 \text{ cm}^2$) of SLG sheets, we used an elastomeric tip array mounted onto the piezoelectric actuators of an atomic force microscope (AFM) to site-specifically apply a force between functionalized cyclopentadienes and SLG sheets. These tip arrays are commonly used for Polymer Pen Lithography, where patterns are formed by ink transfer from the tips to the surface through an aqueous meniscus, resulting in a relationship between dwell time and feature size. Moreover, their large areas ($>1 \text{ cm}^2$) and the computer controlled movement of the piezoactuators that hold the array provide high throughput and flexible pattern design because the elastomeric tips also compress upon contact with surfaces, they can apply a predictable force between molecular inks and a surface. The relationship between applied force and the resulting feature sizes (Eq. 1),

$$F = \frac{(L_f - L_t)E_2 L_t}{\nu} \quad (\text{Eq. 1})$$

where L_f is feature edge length of the top of the tip, L_t is the feature edge length of the bottom of the tip, E_2 is the compression modulus of poly(dimethyl siloxane) (PDMS), and ν is the Poisson's ratio of PDMS, can be used to determine the force between the tips and the surfaces. As a result, in this experimental design, the position, force, and time can all be controlled precisely to pattern surfaces with micrometer scale features over a square centimeter area.

Raman-active cyanine 3 (Cy3) containing cyclopentadiene **1** and electrochemically-active ferrocene cyclopentadienes **2** (Fig. 9c) were designed to characterize the bonding and density upon reaction between the SLG surface and the cyclopentadienes. Cyclopentadienes react quickly in Diels-Alder reactions compared to open chain dienes because they are structurally preorganized for reaction, and as a result, they have been utilized already in the context of surface patterning. Raman spectroscopy has become the standard tool for characterizing chemical modifications onto the basal plane of graphene. The Haddon group observed that following a Diels-Alder reaction onto graphene, the D band at 1345 cm^{-1} that corresponds to the A_{1g} breathing vibration of sp^2 carbon rings, which is suppressed in pure graphene, increases significantly because the introduction of defects or covalently adsorbed molecules reduces the symmetry of the graphene lattice. As a result, the ratio of the D- and G-band intensities (I_D/I_G), determined using the integration of the peaks, is a relative measure of the degree of functionalization of graphene. Alternatively, electrochemistry can confirm the immobilization of the ink onto the surface and quantify the density of surface-bound molecules.

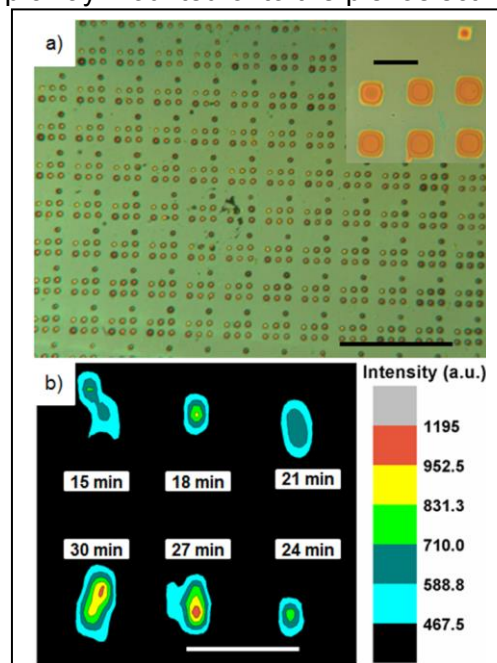


Fig. 10 a) Light microscopy image (10x magnification) of 2 x 3 dot arrays of a mixture containing **1** and PEG with varying dwell times (30, 27, 24, 21, 18, 15 min) were patterned by each pen in the PPL tip array. Scale bar is 200 μm . Inset is a magnified image of one array. Scale bar is 20 μm . b) Raman mapping image (1324 cm^{-1} , D band) of 2 x 3 dot arrays of **1** covalently immobilized onto the SLG. Scale bar is 20 μm .

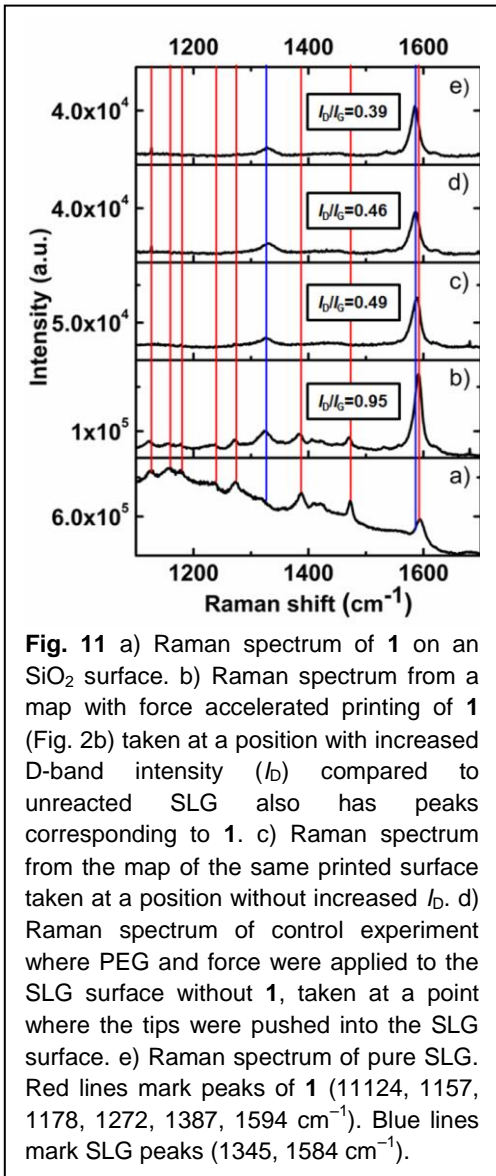


Fig. 11 a) Raman spectrum of **1** on an SiO_2 surface. b) Raman spectrum from a map with force accelerated printing of **1** (Fig. 2b) taken at a position with increased D-band intensity (I_D) compared to unreacted SLG also has peaks corresponding to **1**. c) Raman spectrum from the map of the same printed surface taken at a position without increased I_D . d) Raman spectrum of control experiment where PEG and force were applied to the SLG surface without **1**, taken at a point where the tips were pushed into the SLG surface. e) Raman spectrum of pure SLG. Red lines mark peaks of **1** ($11124, 1157, 1178, 1272, 1387, 1594 \text{ cm}^{-1}$). Blue lines mark SLG peaks ($1345, 1584 \text{ cm}^{-1}$).

revealed a 2×3 pattern of features where I_D was elevated significantly compared to surrounding areas (Figure 10b). The dimensions and feature sizes of these 2×3 pattern, with $20 \mu\text{m}$ spacing between features, matched with the pattern of features printed by the pen array. The elevated I_D was observed at all points where the tips were pressed into the surface for all dwell times. Importantly, control experiments where **1** was not present in the ink mixture or where **1** was present, but force was not applied to the surface upon ink transfer, did not produce similar patterns or significantly elevated I_D/I_G in the Raman maps, confirming that the diene is necessary for changes in bonding to occur. The Raman spectra associated with different points on this map further confirmed that the changes in bonding were produced because of the occurrence of localized Diels-Alder reactions (Figure 11). A Raman spectrum taken at a point where the tips were pressed into the surface had peaks corresponding to the SLG D-band and **1**, as well as an increased I_D/I_G value of 0.95, compared to 0.49 for the unaltered surface, 0.46

Molecules **1** and **2** were synthesized and characterized by ^1H NMR, ^{13}C NMR, and high-resolution mass spectrometry, and all analytical data were consistent with the proposed structures. The 8500 tip arrays with a tip-to-tip spacing of 80 or $160 \mu\text{m}$ were prepared following previously published literature protocols and are composed of PDMS pyramids mounted onto a glass support. To induce the Diels-Alder reaction between **1** and the SLG surface, **1** (0.8 mg, 1.2 mmol) and poly(ethylene glycol) (PEG) (2000 g mol^{-1} , 10 mg mL^{-1}) in 0.8 mL 60 : 20 THF: H_2O , which was sonicated to ensure solution homogeneity, were spin coated (2000 rpm, 2 min) onto a tip array. The PEG matrix that encapsulates the cyclopentadienes ensures even distribution across the tip array, and in the case of Polymer Pen Lithography, transport from the tips to a surface is predictable and reproducible. The tips were then mounted onto the z-piezo of an AFM that was specially equipped with an apparatus to hold the tip arrays, an environmental chamber to regulate the humidity, and customized lithography software to control the position, force, and dwell-time of the tips. A 2×3 dot pattern of **1** with feature-to-feature spacing of $20 \mu\text{m}$ was produced by each tip in the array by pushing the tips into the SLG surface (SLG on 285 nm SiO_2) at times ranging from 15–30 min and a force of $\sim 100 \text{ mN}$ at each spot. The transfer of the **1**/PEG mixture to the surface was confirmed by light microscopy (Figure 10a), and the 2×3 **1**/PEG patterns and the approach dot used to level the tip array with respect to the surface are clearly visible.

After washing the surfaces with EtOH and H_2O to remove unreacted **1** and PEG, the surface bonding was analyzed by Raman microscopy (Renishaw inVia, 633 nm excitation). A Raman map of the surface that was obtained following force accelerated printing of **1**

where the tips had been pressed into the surface in the absence of **1**, and 0.39 for the original SLG surface. The changes in the I_D/I_G in the Raman maps indicate **1** is on the surface and changes in bonding from sp^2 to sp^3 that are consistent with those previously observed for Diels-Alder reactions on SLG surfaces, occur in the same position. Additionally, control experiments confirm that these changes in the spectrum only happen under conditions where the Diels-Alder reaction can proceed. Unlike cycloadditions under pressure, where rate accelerations arise because of the negative activation volume, it is conceivable that rate acceleration may also arise because of the distortions of the SLG π -bonds under applied force that increase their reactivity.

Electrochemically active cyclopentadiene **2** was patterned onto SLG following a similar protocol described above, and the immobilization density of **2** on the SLG surface was analyzed by cyclic voltammetry (CV). Each tip in the pen array produced a 2×3 dot pattern over the 1 cm^2 area covered by the tip array with a dwell time of 30 s at each spot, and ink deposition was confirmed by optical microscopy with an average feature edge length of $7.1 \mu\text{m}$ and area of $50.4 \mu\text{m}^2$.

Following washing of the surface with EtOH and H_2O to remove the PEG and unreacted **2**, CV was carried using a Ag/AgCl reference electrode, a Pt counter electrode, and the patterned SLG as the working electrode. A strong redox peak at $E^\circ = 590 \text{ mV}$ (vs. Ag/AgCl) confirmed the presence of the ferrocene (fc)/ferrocenium (fc⁺) reversible redox couple from **2** (Figure 12), which is shifted anodically compared to fc because of the ester linking the fc to the cyclopentadiene. The linear relationship between peak current and scan rate confirmed that **2** is immobilized on the SLG surface, but that the localized changes in bonding from sp^2 to sp^3 do not prevent conduction through the SLG. However, the difference between oxidation and reduction peaks, ΔE , may indicate an increase in

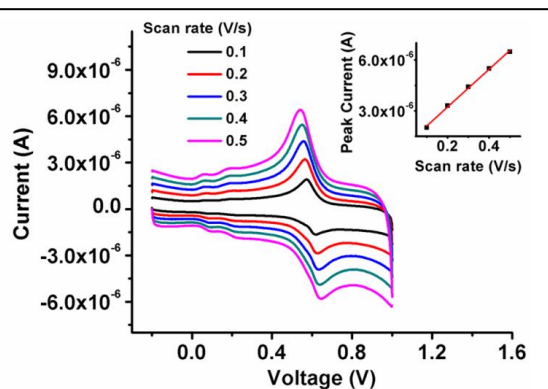


Fig. 12 Cyclic voltammetry (CV) characterization of the SLG patterned with **2** using a Pt counter electrode and Ag/AgCl reference electrode in 0.1 M HClO_4 electrolyte solution. The inset shows the linear relationship between scan rate and current, indicating that **2** is surface immobilized.

resistance upon changes in chemical bonding from sp^2 to sp^3 . The surface density of fc within each feature, Γ_{fc} , was determined from the CV measurements. A Γ_{fc} of $(5.34 \pm 0.76) \times 10^{14} \text{ cm}^{-2}$ was obtained and if the density of π -bonds on the graphene surface is considered, this value of Γ_{fc} corresponds to approximately 29% bond functionalization. Control experiments where **2** was deposited without force did not result in any observable current corresponding to the fc/fc⁺ redox couple after washing, confirming that force is necessary to induce the Diels Alder reaction under these conditions. In conclusion, SLG sheets on SiO_2 substrates have been patterned covalently with organic small molecules through a force-accelerated Diels-Alder reaction induced by an array of pyramidal elastomeric tips. The results of these efforts are described in further detail in an article recently published in the *Journal of the American Chemical Society* (*J. Am. Chem. Soc.* **2013**, *135*, 9240).

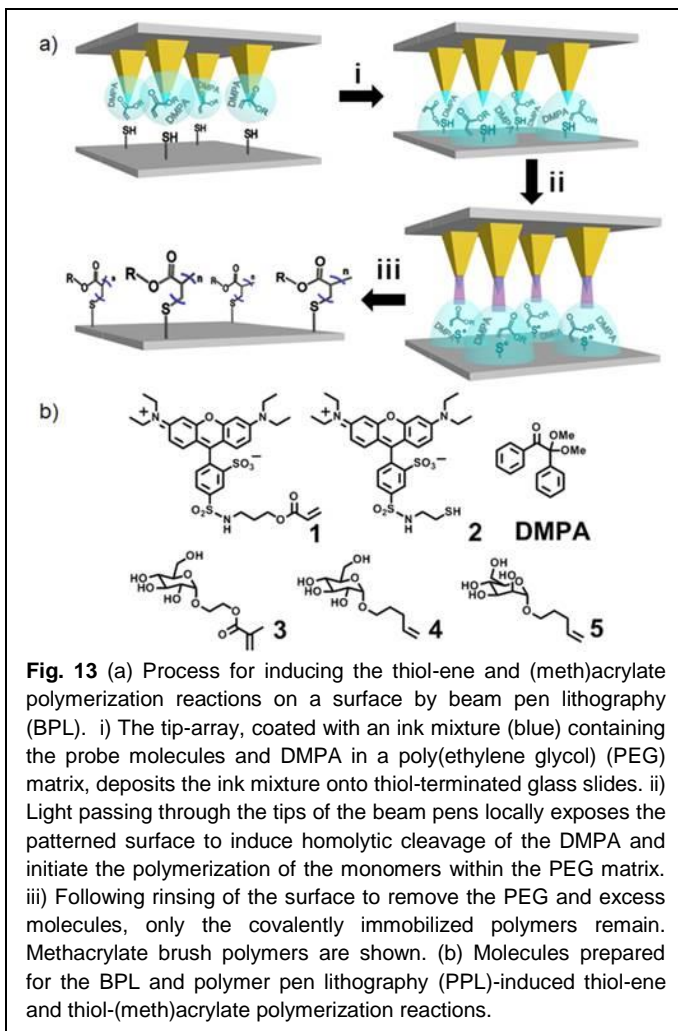


Fig. 13 (a) Process for inducing the thiol-ene and (meth)acrylate polymerization reactions on a surface by beam pen lithography (BPL). i) The tip-array, coated with an ink mixture (blue) containing the probe molecules and DMPA in a poly(ethylene glycol) (PEG) matrix, deposits the ink mixture onto thiol-terminated glass slides. ii) Light passing through the tips of the beam pens locally exposes the patterned surface to induce homolytic cleavage of the DMPA and initiate the polymerization of the monomers within the PEG matrix. iii) Following rinsing of the surface to remove the PEG and excess molecules, only the covalently immobilized polymers remain. Methacrylate brush polymers are shown. (b) Molecules prepared for the BPL and polymer pen lithography (PPL)-induced thiol-ene and thiol-(meth)acrylate polymerization reactions.

C.3. Spatially controlled photochemistry, and its utilization in the synthesis of multivalent glycan arrays

Ideally one would like to generate features that behave as multivalent scaffolds, that can be prepared from readily available starting materials, and that can be patterned using easy to implement surface chemistry. Herein, we describe a new approach that combines PPL or BPL with acrylate or methacrylate photopolymerization chemistry to generate arrays of microscale features of brush polymers that are side-chain functionalized with fluorophores or carbohydrates. These polymers exhibit excellent GBP binding ability by mimicking the multivalent glycan structures typically found on cell surfaces. Using the thousands of tips in a BPL array to localize light on a surface, the exposure time at each position on the surface during the photopolymerization could be varied precisely, providing *in situ* control over polymer length during patterning. Thus, in addition to achieving orders of magnitude improvement over binding sensitivity as a result of multivalency, the glycan arrays prepared by this 3D photolithography demonstrate

that a relationship exists between polymer length and GBP limit of detection.

Inspired by the thiol-ene reaction, which has been used successfully in the context of carbohydrate immobilization, we turned to the thiol-acrylate photopolymerization as a potential route towards creating glycan-functionalized polymer brushes with pendant carbohydrate side groups because of (1) the compatibility of the radical reaction mechanism with the functional groups common to carbohydrates, and (2) the ability to induce the reaction with light made it an appropriate choice for high-throughput processing with BPL. In the presence of the photoinitiator 2,2-dimethoxy-2-phenylacetophenone (DMPA), UV light induces photopolymerization of acrylate or methacrylate monomers from a thiol initiator. By combining this polymerization with BPL arrays, control over feature diameter, feature height and feature spacing was possible. Moreover, the ease with which acrylate and methacrylate monomers are functionalized suggests that this approach could find broad use beyond glycan arrays. However, the photoinduced thiol-initiated acrylate polymerization has not been explored extensively as a tool to synthesize brush polymers, and there are no examples of glycan brush polymers prepared by the thiol-initiated acrylate radical photopolymerization. Therefore before glycan arrays could be synthesized, it was necessary to first develop methods to pattern brush polymers by combining the acrylate photopolymerization reaction with BPL.

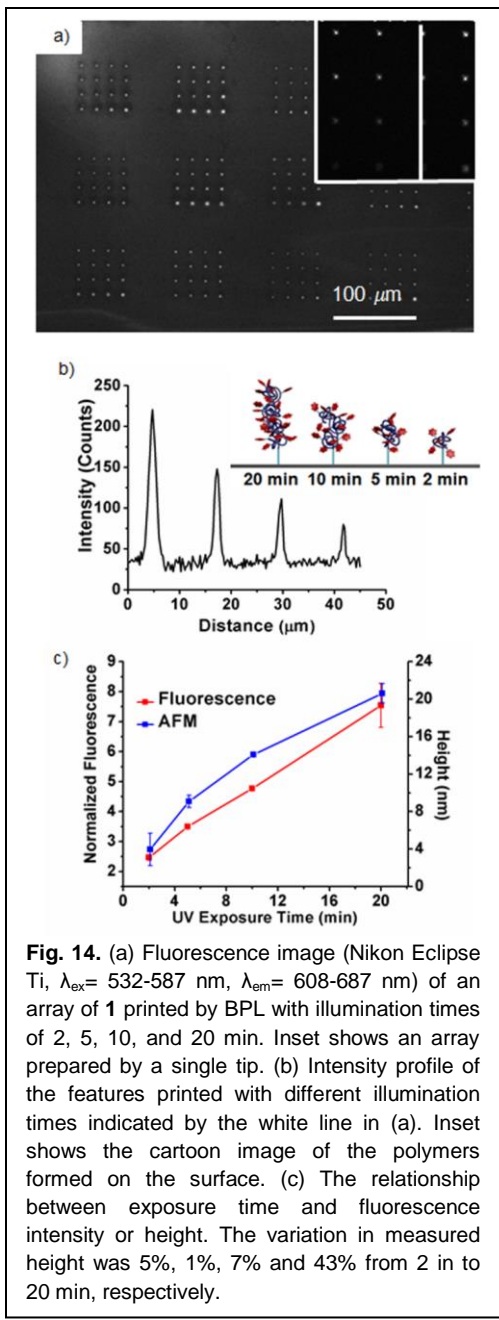


Fig. 14. (a) Fluorescence image (Nikon Eclipse Ti, $\lambda_{\text{ex}} = 532-587 \text{ nm}$, $\lambda_{\text{em}} = 608-687 \text{ nm}$) of an array of **1** printed by BPL with illumination times of 2, 5, 10, and 20 min. Inset shows an array prepared by a single tip. (b) Intensity profile of the features printed with different illumination times indicated by the white line in (a). Inset shows the cartoon image of the polymers formed on the surface. (c) The relationship between exposure time and fluorescence intensity or height. The variation in measured height was 5%, 1%, 7% and 43% from 2 in to 20 min, respectively.

photochemistry is possible through this technique.

Our primary aims in developing this new scanning probe lithography were to create a method to prepare glycan arrays with multivalent carbohydrates and to investigate how molecular architecture affects the binding affinity between patterned glycans and GBPs. We expected, as an important validation of this new approach, that the high glycan valency of our brush polymers would increase significantly the binding towards ConA compared to arrays composed of glycan monolayers. One additional advantage of this new approach is that the pattern versatility enabled by combining BPL with *in situ* glycopolymers synthesis can be used to

The BPL induced radical photopolymerization is a new type of 3D scanning probe nanolithography, where the feature diameter, feature height, feature position can all be controlled independently during printing. The photopolymerization is initiated by photochemical cleavage of the DMPA to form the thiol radical, which in turn initiates acrylate propagation. These thiol radicals, however, lack the stability of conventional radical initiators, and because the chain grows from the thiol, polymerization stops when the light is turned off. Because polymerization proceeds only during illumination, we reasoned that we could use this property of the thiol–acrylate photopolymerization to control brush polymer length by varying the dose of light delivered to each patterned feature. In the current approach, feature position is controlled by the piezoactuator that moves the tip arrays, diameter is varied by the dwell-time between the pen arrays and the surface, and feature height is a function of the irradiation time. To demonstrate the control over feature diameter during thiol–ene and radical polymerization printing, fluorescent molecules **1** and **2** were patterned into a gradient by PPL with dwell times of 50 – 100 000 ms and subsequently irradiated for 3 h (Figure 13). Chain growth, in combination with the inability of thiol-initiators to sustain polymerization in the absence of continuous irradiation, is essential for obtaining precise control over polymer chain length with exposure time. Although chain transfer is likely to occur, chain transfer does not affect the growth kinetics of brush polymers. Thus, 3D lithography capable of immobilizing polymers laden with functional side-chains – while directing feature diameter, feature height, and feature position with sub-micrometer resolution – is achieved by combining BPL with the photoinduced radical polymerization. Importantly, this is the first demonstration of patterning by depositing material with a BPL array followed by exposure, and the first example of covalent photochemistry with BPL, showing that coordinated material deposition and

produce multiplexed arrays of polymers of systematically varied lengths on the same surface. Glucosides **3** and **4** and mannoside **5** were printed by either the thiol–ene or acrylate polymerization reactions onto thiol-terminated glass slides, and the resulting arrays were assayed against solutions containing different concentrations of the GBP concanavilin A (ConA). ConA was selected for these studies because it possesses many of the characteristic binding properties of GBPs that complicate the analysis of GBP–glycan interactions, including (1) multiple recognition sites, (2) cross specificity, and (3) low 1 : 1 binding affinity. Specifically ConA possesses two carbohydrate recognition domains separated by a distance of 6.8 nm and binds both α -mannosides (K_a 10^3 – 10^4 M $^{-1}$) and α -glucosides (K_a 10^2 M $^{-1}$), albeit with a preference for α -mannosides (Figure 14).

The signal for the patterns of the multivalent glucoside **3** that were prepared by the acrylate photopolymerization are approximately 20 times greater than those obtained with amannoside monolayers by the thiol–ene and the CuAAC reactions. Arrays of **3** prepared by the BPL-induced thiol–acrylate photopolymerization decreased steadily with decreasing Cy3-ConA concentration, but still had appreciable signal at 0.43 mM, which is at least one order of magnitude more sensitive than the glycan monolayers prepared by the thiol–ene reaction, and nearly two orders of magnitude more sensitive than α -mannoside monolayers prepared by the CuAAC click reaction (Figure 15). The role of chain length on binding was explored by determining the detection threshold of the different brush polymers of **3**, whose lengths were varied by altering the UV irradiation time. The feature heights of the ConA–brush polymer aggregates increase approximately linearly with exposure time, further supporting the chain growth polymerization mechanism. This work validates three important concepts: (1) the same tips can be used to pattern materials and direct light to them to drive photochemistry, (2) combinatorial covalent photochemistry can be performed using BPL, and (3) arrays of biomaterials constructed through these approaches can be used to address challenging scientific problems, in this case understanding GBP binding. The results of these efforts are described in further detail in an article recently published in *Chemical Science* (*Chem. Sci.* **2014**, 5, 2023).

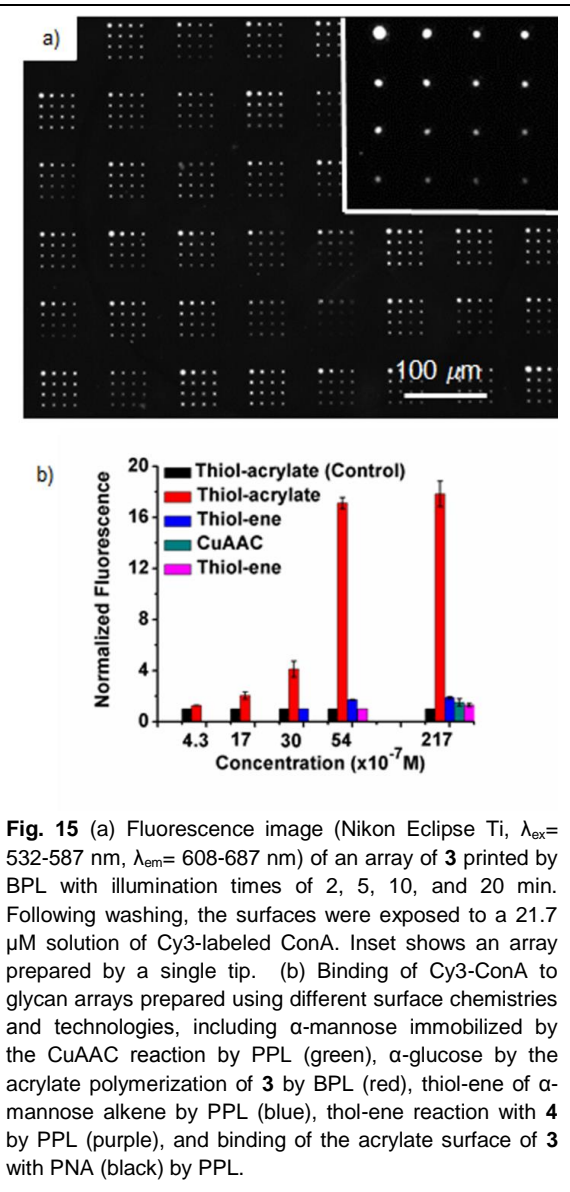


Fig. 15 (a) Fluorescence image (Nikon Eclipse Ti, $\lambda_{\text{ex}}=532$ –587 nm, $\lambda_{\text{em}}=608$ –687 nm) of an array of **3** printed by BPL with illumination times of 2, 5, 10, and 20 min. Following washing, the surfaces were exposed to a 21.7 μM solution of Cy3-labeled ConA. Inset shows an array prepared by a single tip. (b) Binding of Cy3-ConA to glycan arrays prepared using different surface chemistries and technologies, including α -mannose immobilized by the CuAAC reaction by PPL (green), α -glucose by the acrylate polymerization of **3** by BPL (red), thiol-ene of α -mannose alkene by PPL (blue), thol-ene reaction with **4** by PPL (purple), and binding of the acrylate surface of **3** with PNA (black) by PPL.

C.4. Role of Force on the Kinetics of the Huisgen Reaction on Surfaces

The mechanisms by which force accelerates surface reactions remains poorly understood, because there are few experimental methods capable of controlling precisely critical reaction parameters such as reaction time t and applied P . Forces can be controlled accurately using a single AFM tip, but the low throughput of this method necessitates complex single-molecule analyses. Alternatively soft lithography has been used to investigate force-accelerated reactions over large areas, which simplifies analysis, but the applied P is difficult to control. As a result, these AFM and soft lithography experiments can lead to inconsistent and contradictory results. For example, attempts to use force to induce the Huisgen cycloaddition reaction between alkyne-terminated surfaces and azide substrates, or vice versa, in the absence of Cu^+ have alternately concluded that the reaction does and does not proceed under applied pressure. Before the potential of force-induced reactions on surfaces can be realized, there is a need for new experimental methods that can deliver soft organic and biologically active materials onto a surface, apply a controlled localized force, and print over large areas with micrometer scale resolution. We report how arrays composed of approximately 10,000 elastomeric tips mounted on the piezoactuators of an atomic force microscope (AFM) can be used to apply a localized force that accelerates the Huisgen 1,3-dipolar cycloaddition reaction between azide-terminated monolayers and alkyne inks in the absence of the Cu^+ catalyst. Upon bringing the tips into contact with the surfaces, a nanoreactor is formed between the tips and the surfaces that confines the reactants under an applied force (Figure 16). Several aspects of this approach are ideal for patterning applications and for understanding how force and interface structure contribute to the rate constant of reactions, namely (1) these tip arrays uniformly deposit delicate organic and biologically active materials onto surfaces, (2) the piezoelectric tip actuation provides precise control over reaction time and the applied force between the tips and the substrates, and (3) the large patterns (cm^2) created by the massively parallel tip arrays facilitate fluorescence microscopy and electrochemical analysis of the surface reactions. In these studies we show that the rate constant k of the Huisgen reaction on surfaces is sensitively dependent on applied force and, surprisingly, the alkyl chain length of the azide-terminated monolayer.

The CV studies were used to determine the activation volume V_{obs} (observed dependence of $\ln k$ on pressure) by plotting $\ln k$ versus P . An activation volume of $-189 \pm 41 \text{ cm}^3 \text{ mol}^{-1}$ was determined for the Huisgen cycloaddition on the C11 11-azidoundecane-1-thiol SAM. Calculations at the M06-2X/6-31G(d) level in the gas phase show that the (3 + 2) cycloaddition of alkyl azide and terminal alkyne has a V_{f} of about $-13 \text{ cm}^3 \text{ mol}^{-1}$. This value is significantly smaller than that observed in the experiment. We attribute the difference between these two values to the monolayer compression that occurs during printing. We propose that the

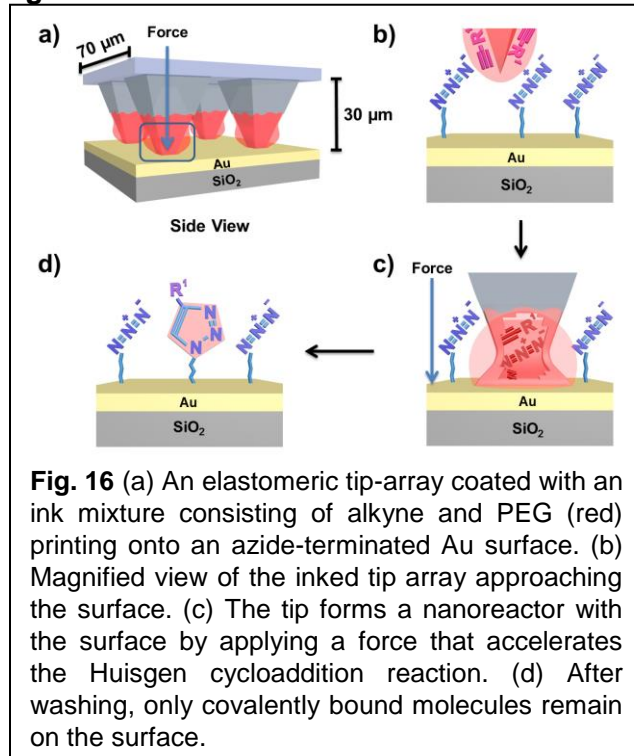
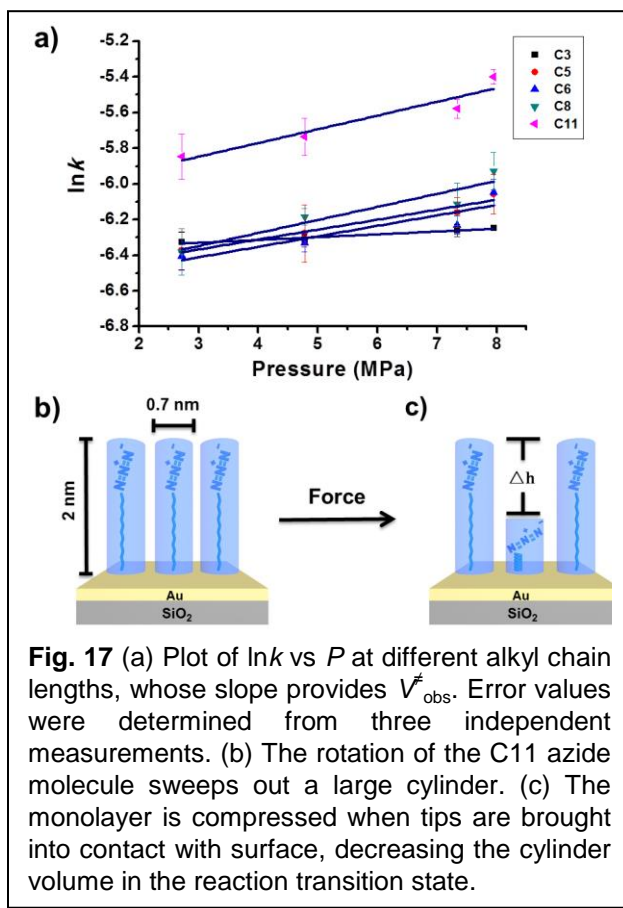


Fig. 16 (a) An elastomeric tip-array coated with an ink mixture consisting of alkyne and PEG (red) printing onto an azide-terminated Au surface. (b) Magnified view of the inked tip array approaching the surface. (c) The tip forms a nanoreactor with the surface by applying a force that accelerates the Huisgen cycloaddition reaction. (d) After washing, only covalently bound molecules remain on the surface.

observed activation volume V_{obs}^* in the nanoreactor is the sum of the activation volume of the cycloaddition reaction V_{c} and the change in the volume of the monolayer

$$\Delta V_{\text{obs}} = \Delta V_{\text{c}} + V_m$$

To test this hypothesis, we reasoned that the height of the monolayer would alter V_{obs}^* because of the differences in the change of ΔV_m during compression. Therefore, **2** was printed on SAMs containing alkane chains of different length between the thiol and the azide with a printing time of 5 min and at pressures of 2.72 – 7.95 MPa (Figure 17). Based on a maximum packing density of 2.7×10^{14} molecules per cm^2 , the measured V_{obs}^* decreases gradually from $-189 \text{ cm}^3 \text{ mol}^{-1}$ for an undecyl chain to $-39 \text{ cm}^3 \text{ mol}^{-1}$ for a propyl chain. This indicates that, assuming that V_{c} remains constant ($-13 \text{ cm}^3 \text{ mol}^{-1}$), the volume change of the monolayer ΔV_m becomes smaller and smaller with the decrease of the height of the monolayer. A simple model can semiquantitatively account for the change in ΔV_m .



The free rotation of the C11 azide molecule on Au in a standing up configuration³⁶ sweeps out a cylinder. From the density of 2.7×10^{14} molecules/ cm^2 of the C11 chain on the surface, the occupied area of the single molecule is calculated to be 0.37 nm^2 . The height of the C11 monolayer is about 2.0 nm, so the volume of the cylinder is 0.74 nm^3 or $445 \text{ cm}^3 \text{ mol}^{-1}$. Calculations indicate that, when two anti-conformers in the middle of the alkane chain are changed to gauche in the reaction, the height of the C11 monolayer decreases to 1.2 nm. This will result in a Δh (Figure 17) of -0.8 nm , leading to an ΔV_m of -0.30 nm^3 or $-178 \text{ cm}^3 \text{ mol}^{-1}$. According to this model, the computed ΔV_m values for the C8, C6, C5, and C3 monolayers are -156 , -134 , -111 , and $-78 \text{ cm}^3 \text{ mol}^{-1}$, respectively, and these data reproduce the trend observed in the experiments. The largest discrepancy between experimental and computational values occurs with the C3 monolayers, which are more likely to lie flat on the substrate and are therefore less compressible along the force vector than the closely packed monolayers used for computations.

In conclusion, we have used massively parallel tip arrays to form nanoreactors that can apply force to accelerate bond forming reactions with negative V_{f} on surfaces. This approach was used to show that the velocity of the Huisgen reaction on surfaces is sensitively dependent on force and monolayer chain length, and a semiquantitative model was developed that explains the previous contradictory results in the literature. Force may have an important role in many interfacial processes, and the approach described in this work can be used to address challenges in materials science, biology, and nanotechnology. The results of these efforts are described in

further detail in an article recently published in the *Journal of the American Chemical Society* (*J. Am. Chem. Soc.* **2014**, *136*, 10553).

C.5. Catalytically Propelled Nanorod Dynamics

A major aim of the proposed work was to couple inorganic nanostructures with the artificial carbohydrate receptors to develop synthetic systems with dynamics and computational complexity similar to biological networks. In Y1, we reported on a new set of equations that describe quantitatively the motion of active catalytic nanorods in H_2O_2 solution (*Physics Review Letters*, **2013**, *110*, 038301). These equations provide a predictive foundation for understanding the motion of real rods possessing defects that are the inevitable result of any nanomanufacturing process,

and therefore accurately predicted the dispersion of activated nanorods by accounting for flipping that occurred as a result of these defects. In Y2 we extended this work by investigating the interactions of these active AuPt nanorods with spherical microparticles to determine how barriers alter the motion of these microswimmers, thereby providing a more complete description of their motion.

We show that, in a suspension of passive spheres on a horizontal surface, self-propelled Au-Pt rods are temporarily trapped and orbit closely around the spheres (Figure 18). These observations are consistent with our model based on lubrication theory, which predicts that swimmers are attracted to obstacles over short distances.

The only key ingredient in the model is a prescribed slip on the swimming surface, a suitable assumption for modeling the motion of a variety of phoretic swimmers and motile ciliates. Thus, the attraction should have broad implications, ranging from the applications of swimmers in synthetic devices to the study of cell adhesion and feeding. We fabricate Au-Pt rods with length $L = 2 \pm 0.2 \mu\text{m}$ and diameter $0.39 \pm 0.04 \mu\text{m}$ following the method of electrochemical deposition in anodic aluminum oxide membranes. The rods and passive spheres with typical diameter $5.5 \pm 0.5 \mu\text{m}$ are suspended in a H_2O_2 solution with typical concentration 15%. The system here is effectively two dimensional because the rods and spheres remain close to the microscope slide. The positions of the rods and spheres are tracked using optical microscopy (Nikon Eclipse 80i, 40X), digital camera (Lumenera Infinity 1-3), and software (ImageJ and Matlab). In the absence of passive spheres, the rods turn, flip, and disperse over time as reported previously. The presence of passive spheres significantly alters the trajectories of self-propelled rods (Figure 18). When a self-propelled rod encounters a sphere, the rod typically orbits around it. The rod

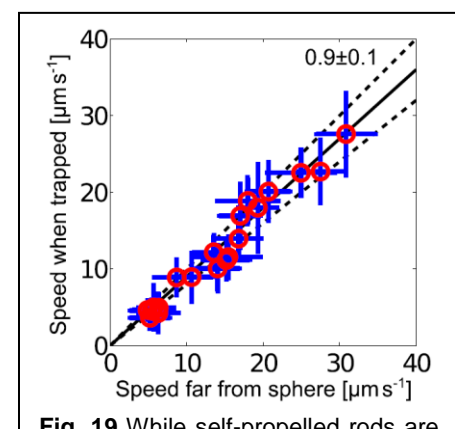


Fig. 19 While self-propelled rods are trapped, they move at speeds comparable to when they are far away from any sphere. Symbols and error bars respectively show the temporal mean and one standard deviation in speed of each rod. Solid and dashed lines have slopes 0.9 ± 0.1 .

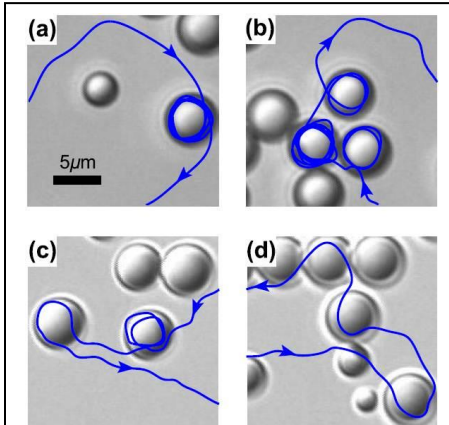


Fig. 18 Sample trajectories of self-propelled rods moving at speeds in the order of $20 \mu\text{m/s}$ near passive spheres. (a) A rod encounters a sphere, orbits around it five times, and moves away. (b) A succession of orbits with the same sense of rotation. (c) The sense of rotation switches. (d) A slalom through a series of spheres.

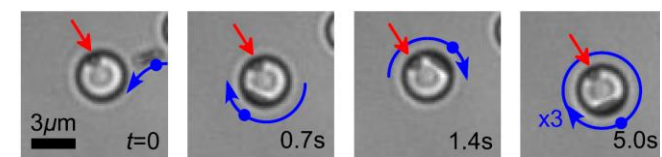


Fig. 20 Image sequence of a solid sphere which hardly rotates while a self-propelled rod orbits around it. The sphere undergoes minor translational diffusion confirming that it is not fixed to the substrate. Red arrows point to a tracer on the sphere. Blue dots and arrows show the location and direction of motion of the rod.

from 1 to 4 μm and spherical beads made of glass, polymerized 3-(trimethoxysilyl)propyl methacrylate (TPM), poly(methyl methacrylate) (PMMA), and polystyrene, ranging in diameter from 1 to 125 μm . Despite differences in chemical and physical properties on their surface, the spheres can trap self-propelled rods in all cases, except for 1 μm polystyrene beads. This exception is attributed to the large sedimentation height of the polystyrene beads which do not remain close to the rods. The self-propelled rods almost maintain their typical speed while they temporarily orbit around spheres (Figure 19). This shows that the rods hardly experience any additional drag despite moving close to the solid spheres. While a rod is trapped, it remains in a narrow region between the sphere and the surface (Figure 20), whose height is estimated to be ~ 550 nm after accounting for minor optical aberrations. This height is not much greater than the rod diameter, meaning that the rods orbit closely around spheres.

Do spheres rotate while a rod orbits around them? To answer this question, we use inert PMMA spheres with an embedded piece of hematite acting as a black marker. The marker remains almost stationary while a rod orbits around a sphere (Figure 21). The sphere is almost always detached from the moving rod, suggesting that any collision occurs only briefly. This is the first experimental evidence supporting the previous hypothesis that the rods generate a local flow along their surface, as elaborated further in our theory below. There are several possible mechanisms of trapping. The rods are slightly curved and tend to move in curved paths with typical curvature $\kappa \sim 0.12 \mu\text{m}^{-1}$ so they could slide along at and curved surfaces with curvature much less than κ . However, we observe rods orbiting around glass spheres with diameter as small as 1 μm , which has curvature much greater than κ . Long-range hydrodynamic attraction towards a surface is possible for swimmers that are represented by a force dipole with positive strength (pusher), though our rods experience only short-range attraction towards spheres as

can move around a succession of spheres and either continue to turn in the same sense or switch handedness of circular motion. The trajectory may deflect only slightly when the rod is close to a sphere, but the direction is always towards the sphere.

This phenomenon of self-propelled rods orbiting around spheres occurs over a wide range of materials and sizes. We observe rods ranging in length

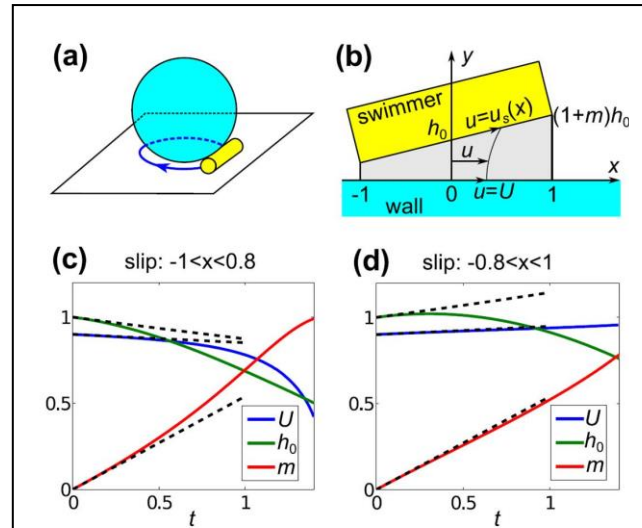


Fig. 21 (a) Sketch of a rod orbiting around a sphere on a horizontal surface. (b) Theoretical configuration of a swimming body near a rigid wall in the reference frame of the swimmer. The wall approximates the local surface of the sphere and translates to the right. (c,d) Predictions for the swimming speed U , distance h_0 away from the wall, and rescaled slope m of a swimmer with constant slip velocity prescribed on 90% of the front or back of the body. Dashed lines show the early-time regime.

confirmed below. The attraction could be a consequence of short-range hydrodynamic interactions much like between bacteria and walls. The short-range interactions between rods and spheres are studied further by formulating a two-dimensional model of a rod moving horizontally near a wall. While our experimental system is three dimensional with curved boundaries, our simplified model approximates the local surface of the spherical obstacle by a flat immobile wall. Thermal fluctuations are neglected for simplicity. We adopt a Cartesian coordinate system (x, y) in the reference frame that translates with the swimmer along the wall, where x is scaled by a half of the length of the swimming body $L=2$ and y is scaled by a typical distance H between the swimmer and the wall (Fig. 16b). In this moving reference frame, the wall is represented by $y = 0$ and translates to the right with speed U , where all speeds are scaled by a typical slip velocity V on the swimmer. The wall-facing surface of the swimmer is represented by $y = h$ with $h = h_0(1 + mx)$, where h_0 is a re-scaled distance from the wall to the mid-point of the swimming surface and m is a re-scaled slope of the swimmer relative to the wall. Note that $m = 1$ corresponds to the front end of the swimmer hitting the wall. The aim is to

predict how U , h_0 , and m evolve over time, given a prescribed slip speed u_s on the surface of the swimmer.

To verify experimentally that only short-range interactions occur between self-propelled rods and passive spheres, we consider the effective density of a suspension of rods as a function of the distance away from the lowest point of a sphere (Figure 22). This is measured by sampling the distance from a specified rod to the nearest sphere over time, excluding cases when the rod has multiple spheres within three radii of the sphere. For passive rods in water, the density is almost uniform everywhere except below the sphere, where the density decreases to zero. For active rods in H_2O_2 , the density is almost

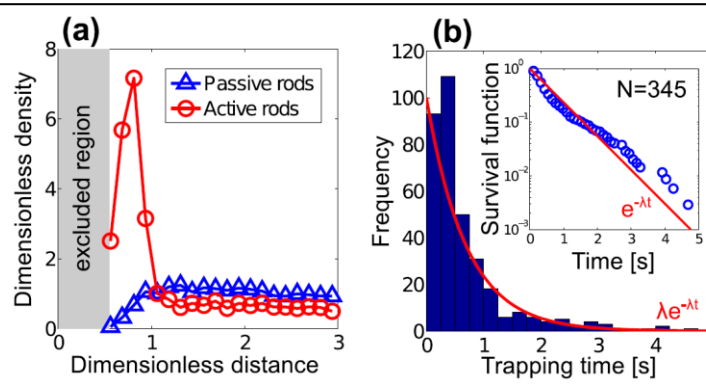


Fig. 22 (a) Experimental data of the effective density of a suspension of rods, scaled by the expectation if the rods were distributed uniformly. This is plotted against the distance from the lowest point of a sphere in units of the sphere radius, based on over 4000 measurements of the distance over time. Below the sphere, the density of passive rods falls while the density of self-propelled rods peaks. The excluded region is where the rods are physically unable to enter. (b) Histogram of trapping times of self-propelled rods orbiting around spheres. Inset shows the probability that the rods remain trapped beyond a specified time. Red curves are exponential distributions with rate parameter $\lambda = 1.5 \text{ s}^{-1}$.

uniform everywhere except below the sphere again, where the rods are now highly concentrated. This supports our theory that moving rods remain trapped primarily because of short-range hydrodynamic effects.

To explore why the rods eventually move away from the spheres, we observe that the trapping times are typically less than 5 seconds and that their distribution shows an exponential decay with rate $\lambda=1.5 \text{ s}^{-1}$ (Figure 22). In rare instances, the rods remain trapped for longer times in the order of minutes. Highly curved rods that move in small circles tend to either remain trapped for relatively long times or hardly remain trapped, depending on whether they approach a sphere with the trajectory curving towards or away from the sphere, respectively. Perhaps the rods are curved towards the sphere while they are trapped until fluctuations flip them over and enable them to escape, suggesting that rod curvature and flipping affect the movement of rods near spheres. Thermal fluctuations are most likely to be driving the rods away from remaining

trapped, since the time scale associated with trapping λ^{-1} is comparable to the time scales of rotational diffusion and duration between stochastic flips, which are both in the order of one second. While our deterministic model predicts that swimmers move closer to a confining surface, fluctuations may cause the swimmers to move away or remain at a characteristic distance from the surface. This may explain why self-propelled rods appear to move closer to the substrate than the expected sedimentation height of purely diffusive rods. The exact distance between swimmers and confining boundaries could be predicted in the future by extending our model to incorporate the effects of fluctuations, gravity, and the curvature of the swimmers and boundaries.

The short-range attraction towards walls has broad implications on potential applications of synthetic swimmers as well as addressing the behavior of motile cells. Many swimmers including motile ciliates and synthetic phoretic particles could be interpreted to have an effective slip on a majority of their surface. Our model suggests that these swimmers accumulate along boundaries, contrary to passive particles which have difficulty diffusing into spatially constricted regions. This may offer insight into the possible hydrodynamic effects in cell adhesion and feeding, as well as suggest strategies to capture and filter groups of swimmers using synthetic devices. Our model also implies that, while the swimmers may not mix fluids over long distances, payloads attached to the swimmers may exert more drag and perhaps develop large-scale flow patterns as observed in bacterial baths. Short-range interactions between swimmers and obstacles importantly affect their movements and must be incorporated in any accurate model of self-propelled colloidal suspensions, and will be particularly important when using these systems to understand how carbohydrate recognition can influence the assembly of dynamic nanostructures. The results of these efforts are described in further detail in an article recently published in *Soft Matter* (*Soft Matter* **2014**, *10*, 1784).

C.6. Summary of Accomplishments

In summary, this award from the AFOSR has directly supported several major research accomplishments that will lead to the creation of carbohydrate-based nanotechnology. Specifically, we have created a synthetic lectin that employs cooperativity to obtain selectivity for mannose and characterized the thermodynamics of binding and the structure of this receptor when bound to several monosaccharides. *This work is a major breakthrough because, while cooperativity is ubiquitous in the binding of carbohydrates in nature, our work is the first example that demonstrates cooperativity in a synthetic carbohydrate receptor.* Another major accomplishment is that we have developed new tools and techniques to create glycan arrays, including a photochemical approach that leads to glycopolymers that are orders of magnitude more sensitive towards lectins than glycan arrays prepared by other methods. In the course of these studies, we have also increased the understanding of reactivity of surfaces in several important ways, including developing the first method to covalently pattern graphene through a force-accelerated Diels-Alder reaction and also developed a new quantitative understanding of how force affects reactivity on self-assembled monolayers. Finally, we have developed a quantitative description for the motion of catalytic Au-Pt nanoswimmers that explain their diffusion and interaction with barriers. Taken together, these results demonstrate the potential of carbohydrates as directing elements in advanced nanotechnologies and provide a strong foundation for developing this transformational research area.

D. Personnel Supported

Personnel Supported	Percentage of Salary Provided by Grant	Period
Braunschweig, Adam (PI)	8.3 %	(7/1/2013 – 6/30/2014)
Guzman, Carmen X. (Graduate Student)	20.2%	(7/1/2013 – 6/30/2014)
Guchhait, Tapas (Postdoc)	100%	(8/1/2013 – 10/31/2013)
Ley, David (Postdoc)	1%	(7/1/2013 – 6/30/2014)
Munro, Catherine (Graduate Student)	12%	(7/1/2013 – 6/30/2014)
Zheng, Yeting	12%	(7/1/2013 – 6/30/2014)
Ji, Yiwen	12%	(7/1/2013 – 6/30/2014)
Han, Xu	12%	(7/1/2013 – 6/30/2014)

E. Publications

1. Bian, S.; He, J.; Schesing, K. B.; Braunschweig, A. B.* "Polymer Pen Lithography (PPL) Induced Site-Specific Click Chemistry for the Formation of Functional Glycan Arrays" *Small*, **2012**, 8, 2000–2005. DOI: 10.1002/smll.201102707.
2. Bian, S.; Schesing, K. B.; Braunschweig, A. B.* "Matrix-assisted Polymer Pen Lithography induced Staudinger Ligation" *Chem. Commun.* **2012**, 48, 4995 – 4997. DOI: 10.1039/C2CC31615C.
3. Rieth, S.; Miner, M. R.; Chang, C. M.; Hurlocker, B.; Braunschweig, A. B.* "Saccharide Receptor Achieves Concentration Dependent Mannoside Selectivity Through Two Distinct Cooperative Binding Pathways" *Chemical Science*, **2013**, 4, 357–367. DOI: 10.1039/C2SC20873C.
4. Takagi, D.; Braunschweig, A. B.; Zhang, J.; Shelley, M. J. "Dispersion of Self-Propelled Rods Undergoing Fluctuation-Driven Flips" *Physics Review Letters*, **2013**, 110, 038301. DOI: 10.1103/PhysRevLett.110.038301.
5. Zhong, X.; Bailey, N. A.; Schesing, K. B.; Bian, S.; Campos, L. M.;* Braunschweig, A. B.* "Materials for the Preparation of Polymer Pen Lithography Tip Arrays and a Comparison of their Printing Properties" *Journal of Polymer Science A: Polymer Chemistry*, **2013**, 51, 1533 –1539. DOI: 10.1002/pola.26513. **Journal Cover**.
6. Bian, S.; Scott, A. M.; Cao, Y.; Liang, Y.; Osuna, S.; Houk, K. N.; Braunschweig, A. B.* "Covalently Patterned Graphene Surfaces by a Force Accelerated Diels-Alder Reaction" *Journal of the American Chemical Society*, **2013**, 135, 9240 – 9243. DOI: 10.1021/ja4042077. • Highlighted in *Chemical and Engineering News*, 25 June 2013, vol 91(26), p6. • Highlighted in *Science*, **2013**, 341, 320. • JACS spotlight
7. Takagi, D.; Palacci, J.; Braunschweig, A. B.; Shelley, M. J.; Zhang, J. "Synthetic Microswimmers Orbit Closely Around Spherical Obstacles" *Soft Matter*, **2014**, 10, 1784–1789. DOI: 10.1039/C3SM52815D.
8. Bian, S.; Zieba, S. B.; Morris, W. M.; Xu, H.; Richter, D. C.; Brown, K. A.; Mirkin, C. A.; Braunschweig, A. B.* "Beam Pen Lithography as a New Tool for Spatially Controlled Photochemistry, and its Utilization in the Synthesis of Multivalent Glycan Arrays" *Chemical Science*, **2014**, 5, 2023 – 2030. DOI:10.1039/C3SC53315H.
9. Han, X.; Bian, S.; Liang, Y.; Houk, K. N.; Braunschweig, A. B.* "Reactions in Elastomeric Nanoreactors Reveal the Role of Force on the Kinetics of the Huisgen Reaction on Surfaces" *Journal of the American Chemical Society*, **2014**, 136, 10553–10556. DOI: 10.1021/ja504137u.

F. Presentations

14. **ACS Florida Annual Meeting and Exposition, Tampa, Florida, 8 May 2014, Keynote Address, Materials Division**
Two Examples Demonstrating the Importance of Surface Organic Chemistry: Photochemically- and Force-Initiated Brush Polymer Microarrays
13. **247th American Chemical Society National Meeting, Dallas, Texas, 20 March 2014**
“Glycan Microarrays Prepared via a Beam Pen Lithography Induced Thiol-Acrylate Photopolymerization”
12. **21st New Orleans Carbohydrate Symposium, New Orleans, LA, 21 March 2014**
“New Tools for the Preparation of Multivalent Glycan Nanoarrays”
11. **247th American Chemical Society National Meeting, Dallas, TX**
Polymeric Materials: Science and Engineering Young Investigator’s Symposium
“Photochemically- and Force-Initiated Brush Polymer Microarrays and Their Applications in Sensing and Electronic Materials”
10. **AFOSR Natural Material and Systems Program Review, Fort Walton, FL, December 13, 2013**
“Carbohydrate Nanotechnology: Multivalency, Logic, Organization”
9. **CUNY Brooklyn, Department of Chemistry, Department Colloquium, November 21, 2013**
“Photochemically- and Force-Initiated Brush Polymer Microarrays and Their Applications in Sensing and Electronic Materials”
8. **Florida International University, Department of Physics, Department Colloquium**
“The Potential of Massively Parallel Tip Arrays in Biological Microarrays and Electronics”
7. **8th International Symposium on Macrocyclic and Supramolecular Chemistry, Washington D.C., June 2013**
“Accessing Molecular Complexity With Conformationally Dynamic Synthetic Carbohydrate Receptors”
6. **Departmental Seminar SUNY Stony Brook, February 8, 2013**
Carbohydrate Nanotechnology and Self-Assembling Complexity: Beyond Binary Solutions to Molecular Logic
5. **University of Miami, Department of Chemistry, February 21, 2012**
“A Mannose-Selective Synthetic Receptor With a Unique Cooperative Binding Mechanism”
4. **AFOSR Natural Material and Systems & Extremophiles Program Review, Washington D.C.**
“Carbohydrate Nanotechnology: Hierarchical Assemblies and Information Processing with Oligosaccharide Host-Guest Systems”
3. **244th American Chemical Society National Meeting, Philadelphia, PA**
“Using Polymer Pen Lithography to create new covalent bonds on surfaces with submicrometer feature diameters”
2. **244th American Chemical Society National Meeting, Philadelphia, PA**
“Synthetic carbohydrate receptors achieve specificity through positive allosteric cooperativity”
1. **244th American Chemical Society National Meeting, Philadelphia, PA**
“Matrix-assisted Polymer Pen Lithography: A new method for immobilization of bioorthogonal reactions and kinetic characterization of force catalyzed reactions”

G. Student Theses Defended

Bian, Shudan, PhD Thesis, "Massively Parallel Tip Arrays As Tools To Gain New Insights Into Organic Reactions On Surfaces"

H. Consultative/Advisory Functions

1. Manuscript Reviewer: *Accounts of Chemical Research, ACS Applied Materials and Interfaces, ACS Macro Letters, ACS Nano, Applied Physics A: Materials Science & Processing, Beilstein Journal of Organic Chemistry, Chemical Communications, Chemical Science, Chemistry – An Asian Journal, Chemistry – A European Journal, Journal of the American Chemical Society, Journal of Applied Polymer Science, Journal of Nanobiotechnology, Macromolecules, Nature Chemistry, Nature Nanotechnology, RSC Advances, Small, Supramolecular Chemistry*.
2. Proposal Review: National Science Foundation BIO Review Panel; Army Research Office; Air Force Office of Scientific Research, Louisiana Board of Regents
3. Consulting: Applied Minerals, LLC

I. New Invention Disclosures and Patents

1. **Braunschweig, A. B.**; He, Jiajun; Bian, S.; Schesing, K. B. "Nanoreactor Printing" Non-Provisional Patent Application *PCT/US12/32019*
2. **Braunschweig, A. B.**; Rieth, S.; Miner, M. R. "Carbohydrate Selective Receptors" Provisional Patent Application
3. **Braunschweig, A. B.**; Bian, S. "Covalently Patterned Graphene by a Force Accelerated Cycloaddition Reaction" Non-Provisional Patent Application *PCT/US13/44570*

J. Honors/Awards

American Chemical Society (ACS) Polymeric Materials: Science and Engineering (PMSE) Young Investigator Award